NeuroImage 208 (2020) 116434

Contents lists available at ScienceDirect

NeuroImage

journal homepage: www.elsevier.com/locate/neuroimage

Impact of prospective motion correction, distortion correction methods and large vein bias on the spatial accuracy of cortical laminar fMRI at 9.4 Tesla

Jonas Bause [a,b,c,*], Jonathan R. Polimeni [d,e], Johannes Stelzer [a,b], Myung-Ho In [f], Philipp Ehses [g], Pablo Kraemer-Fernandez [h], Ali Aghaeifar [b,c], Eric Lacosse [b,i], Rolf Pohmann [b], Klaus Scheffler [a,b]

[a] Department for Biomedical Magnetic Resonance Imaging, University Hospital Tuebingen, Germany
[b] High-Field Magnetic Resonance Center, Max Planck Institute for Biological Cybernetics, Tuebingen, Germany
[c] Graduate School of Neuronal and Behavioral Sciences, University of Tuebingen, Tuebingen, Germany
[d] Athinoula A. Martinos Center for Biomedical Imaging, Department of Radiology, Harvard Medical School, Massachusetts General Hospital, Charleston, MA, USA
[e] Harvard-MIT Division of Health Sciences and Technology, Massachusetts Institute of Technology, Cambridge, MA, USA
[f] Department of Radiology, Mayo Clinic, Rochester, MN, USA
[g] German Center for Neurodegenerative Diseases (DZNE), Bonn, Germany
[h] Department of Prosthodontics, University Hospital Tuebingen, Tuebingen, Germany
[i] Autonomous Learning Group, Max-Planck Institute for Intelligent Systems, Tuebingen, Germany

ARTICLE INFO

Keywords:
Laminar fMRI
Gradient echo EPI
Prospective motion correction
Distortion correction
Ultra-high field
Macro-vascular bias

ABSTRACT

Functional imaging with sub-millimeter spatial resolution is a basic requirement for assessing functional MRI (fMRI) responses across different cortical depths and is used extensively in the emerging field of laminar fMRI. Such studies seek to investigate the detailed functional organization of the brain and may develop to a new powerful tool for human neuroscience. However, several studies have shown that measurement of laminar fMRI responses can be biased by the image acquisition and data processing strategies. In this work, measurements with three different gradient-echo EPI BOLD fMRI protocols with a voxel size down to 650 μm isotropic were performed at 9.4 T. We estimated how prospective motion correction can help to improve spatial accuracy by reducing the number of spatial resampling steps in postprocessing. In addition, we demonstrate key requirements for accurate geometric distortion correction to ensure that distortion correction maps are properly aligned to the functional data and that strong variations of distortions near large veins can lead to signal overlays which cannot be corrected for during postprocessing. Furthermore, this study illustrates the spatial extent of bias induced by pial and other larger veins in laminar BOLD experiments. Since these issues under investigation affect studies performed with more conventional spatial resolutions, the methods applied in this work may also help to improve the understanding of the BOLD signal more broadly.

1. Introduction

An increasing number of studies aim to perform functional MRI (fMRI) measurements acquired at ultra-high field (UHF) with voxel dimensions in the sub-millimeter scale. Such studies are possible primarily due to the stronger BOLD effect at higher fields (Scheffler et al., 2019; Turner et al., 1993), resulting in an increased contrast-to-noise ratio (CNR) in fMRI, as well as the superlinear increase of image signal-to-noise ratio with field strength (Pohmann et al., 2016). The enhanced resolution afforded by these sensitivity gains allows detailed investigation of the BOLD response in varying depths of cortical gray matter, which has rapidly developed to a new field of research. Although the spatial resolution is still too coarse to be actually capable of resolving individual cytoarchitectonically defined cortical layers, this is often referred to 'laminar' or 'depth-dependent' fMRI and aims for a better understanding of the role of individual cortical layers in, for example, feed-forward and feed-back processing (Lawrence et al., 2017). Smaller voxel dimensions additionally help to differentiate between macro- and microvascular signal sources due to reduced partial volume effects and physiological noise contributions (Triantafyllou et al., 2005). As voxels become smaller, the heterogeneity of vessel sizes within a given voxel decreases, which can allow for a better understanding of how the different stages of the vascular hierarchy contribute to the observed fMRI signal. Although laminar fMRI studies employing BOLD contrast have

* Corresponding author. Max-Planck-Ring 11, 72076, Tuebingen, Germany.
E-mail address: jonas.bause@tuebingen.mpg.de (J. Bause).

https://doi.org/10.1016/j.neuroimage.2019.116434
Received 18 April 2019; Received in revised form 8 November 2019; Accepted 2 December 2019
Available online 6 December 2019

been performed using different pulse sequences (e.g. 2D (Siero et al., 2015) and 3D gradient-echo (GE) echo-planar-imaging (EPI) (Fracasso et al., 2017), 2D (Kashyap et al., 2018) and 3D FLASH (Koopmans et al., 2011) as well as 2D spin-echo EPI (Goense et al., 2012), 3D GRASE (Kemper et al., 2015) and SSFP (Goa et al., 2014)), in this study we focus on 2D GE-EPI because it provides fast imaging speeds with high SNR efficiency and is the most common readout in fMRI.

In order to reduce the influence of motion in fMRI analyses, retrospective motion correction (RMC) is commonly applied during post-processing (Friston et al., 1996). However, these algorithms typically assume that subject motion can be described as rigid body displacement of the complete volume, thereby neglecting the sequential acquisition of individual slices in 2D imaging (Oakes et al., 2005). Retrospective motion correction also cannot account for spin history effects, which induce signal intensity fluctuations during motion and thereby reduce statistical power (Muraskin et al., 2013), or may even misinterpret BOLD effect related signal changes as motion (Schulz et al., 2014). Another limitation of RMC in partial brain fMRI studies is that signal from brain regions near the border of the imaging volume that move outside of the volume cannot be recovered. Like many postprocessing steps, RMC requires spatial image resampling, and any image resampling involves signal interpolation from the neighboring voxels which leads to spatial blurring that is dependent on the direction and amount of motion (Polimeni et al., 2018). Some of the issues can be addressed by updating the slice orientation and position during the experiment using motion estimates from the acquired image data (Thesen et al., 2000). However, it would be desirable for the motion correction performance to be completely independent of image quality and the field-of-view (FOV). This requires measurement of subject motion in real-time and the correction of the individual slice positions independent of the actual imaging sequence. Several approaches for prospective motion correction (PMC) have been presented (for detailed reviews, see (Maclaren et al., 2013; Zaitsev et al., 2017)). A method that provides high accuracy does not require additional RF pulses or gradients and needs only minor sequence modifications is motion tracking with camera systems built into the MRI bore, which can capture the position of dedicated markers attached, for example, to an occlusal splint (Maclaren et al., 2012; Zaitsev et al., 2006). Furthermore, PMC can correct between-scan motion and thus perfectly align different runs or functional and reference/anatomical measurements. Nevertheless, the performance of PMC for sub-millimeter fMRI studies has, to the authors knowledge, so far not been characterized.

In 2D-EPI acquisitions at UHF, the strong static magnetic field (B_0) inhomogeneities, which neither shim coils built in the gradient system nor dedicated shim coil arrangements can sufficiently correct (Aghaeifar et al., 2018; Stockmann et al., 2015), often lead to geometric or even signal dropouts in case of through slice dephasing. Conventionally, geometric distortions are reduced by decreasing the echo spacing (ES) between two adjacent reconstructed k-space lines using parallel imaging at the cost of lower SNR (Griswold et al., 2002; Pruessmann et al., 1999). Additionally, parallel imaging enables reduction of the echo time (TE) and the overall readout duration which may be desirable in order to optimize the functional contrast and minimize signal blurring. Another possibility to decrease distortions and TE provides the utilization of segmented-accelerated sampling schemes (Berman et al., 2019) or reduced FOV imaging by decreasing the number of phase-encoding steps. For the latter, selective excitation (Finsterbusch, 2013) or signal saturation in the area outside of the region of interest can be used (Pfeuffer et al., 2002a) in order to prevent aliasing artifacts. Although the foremost approach is more time efficient and typically less SAR intense, strong inhomogeneities in the static and transmit field make selective excitation challenging at UHF. In contrast, the combination of zoomed GE-EPI with GRAPPA (generalized autocalibrated partially parallel acquisitions (Griswold et al., 2002),) was successfully demonstrated in almost distortion free single-shot GE-EPI with 0.65 mm isotropic resolution at 7 T (Heidemann et al., 2012).

To ensure adequate alignment of functional with anatomical reference data, as typically required to determine the corresponding cortical depth for each fMRI voxel, all geometric distortions need to be corrected. Beyond macroscopic field inhomogeneities, susceptibility differences near large veins and the resulting distortions may make it difficult to precisely assign the cortical depths, but are usually not considered relevant since the artifacts are more subtle and may only affect studies using sub-millimeter voxel sizes. The most prominent correction techniques are based on B_0 field maps (Reber et al., 1998), measurements with reversed phase-encoding directions (Andersson et al., 2003), multi-reference methods (Wan et al., 1997) and the point spread function (PSF) method (Robson et al., 1997; Zaitsev et al., 2004; Zeng and Constable, 2002). In the PSF method, a modified EPI sequence with an additional phase-encoding is used to map geometric distortions. Since the same readout is used for the distortion mapping as in the functional experiment, influences of eddy currents and chemical shift effects are captured as well. The duration of the additional reference scan can be shorten by using reduced field of view sampling (rFOV) or parallel imaging along the PSF encoding dimension (In and Speck, 2012; Zaitsev et al., 2004).

Already in early laminar fMRI studies, increasing gradient-echo BOLD signal amplitudes towards the cortical surface were observed (Polimeni et al., 2010; Ress et al., 2007; Siero et al., 2011) and usually interpreted as extravascular BOLD changes evoked by nearby pial veins (Turner, 2002). At the same time, intra-vascular signal changes can typically not be observed at high-field GE-EPI measurements due to the rapid decay of the venous blood signal. Although efforts have been made to avoid this venous bias by employing vessel masks (Koopmans et al., 2010) or regressing the signal amplitude variation across depths (Fracasso et al., 2017), it is desirable to achieve a better understanding of the spatial extent of this effect and to characterize how far this pial BOLD signal penetrate into the parenchyma. Progress towards this characterization has been made by a recent study (Kay et al., 2018) which demonstrated the distinct relationship of proximal large veins and BOLD signal in tangential profiles along the cortex.

Several of the abovementioned challenges of image acquisition and data processing have been described previously in several review articles (Kemper et al., 2018; Petridou and Siero, 2017; Polimeni et al., 2018). In this study, we examine the specific influences of spatial resolution and readout duration for high-resolution fMRI studies, assess the within-scan and across-scan motion measured by a prospective motion correction system and the detectable residual image displacements. Furthermore, we compare the interpolation-induced blurring for geometric distortion correction with the PSF and B_0 mapping method. Moreover, BOLD responses are studied as a function of large vein distance and cortical depth in order to address the question whether the functional signal increase towards cortical surface is primarily caused by the proximity to large veins.

2. Methods

2.1. Image acquisition

The study was approved by the local ethics committee (University Tuebingen, Germany) and all four subjects (23–32 years old) gave written informed consent before being scanned. Experiments were performed on a 9.4 T MRI Scanner (Siemens Healthineers, Germany) equipped with a whole-body gradient system and an in-house developed transmit coil having two rows with eight transmit channels each (Shajan et al., 2013). The coil was driven with a static phase shim in positive circular-polarization (CP^+) mode (45° phase shift between adjacent elements within each row) and combined with a 31 channel receive array. During all experiments, the subjects were instructed to move as little as possible, and head motion was physically restricted by foam pads. The reference transmit voltage was determined for the occipital lobe by measuring the achieved flip-angle using an actual flip-angle imaging sequence (AFI (Yarnykh, 2007)) with a voxel size of 3.3 mm isotropic and full brain coverage.

2.1.1. Zoomed gradient-echo EPI sequence

For outer volume suppression, a 37.2 ms long asymmetric adiabatic full passage pulse (Hwang et al., 1999) in conjunction with spoiler gradients, was implemented in a standard GE-EPI sequence and a point spread function mapping sequence, respectively. As suggested by (Speck et al., 2008), additional fat saturation pulses were omitted. The required auto-calibration scans for the GRAPPA reconstruction were measured with the fast low excitation echo-planar method (FLEET (Polimeni et al., 2016)), in which the outer volume suppression pulse was played out before each segment in order to avoid aliasing of fast relaxing components. To avoid an excessively high power deposition in a short period of time during the FLEET pre-scan, the inter-segment repetition time (TR) was set to the same value as the temporal spacing between successive slice excitations in the accelerated component of the sequence (volume TR/number of slices = 117.6 ms).

The head positions and orientations of the subjects were measured and corrected in real-time by updating the gradients accordingly for all functional measurements. The position measurements were performed with an optical tracking system (specifications: frame rate = 84 Hz, translational accuracy < 0.1 mm, rotational accuracy < 0.05°, KinetiCor Inc., USA) mounted to the ceiling of the magnet bore. In order to decrease potential errors caused by vibrations, a moving average filter over the latest five camera measurements was applied. The camera tracked the position of a moiré pattern marker which was fixed to a tight fitting occlusal splint individually built for each subject by the local dental clinics. The marker position was then streamed continuously to the scanner host via an UDP connection where the new slice position was calculated and updated by adapting the gradients accordingly (Aghaeifar et al., 2017). In order keep all functional measurements aligned, the initial position at the beginning of the first EPI run of the session was taken as a reference for all subsequent EPI measurements.

2.1.2. EPI measurements

Before the first EPI measurement of each session, three automatic B_0-shimming iterations (up to 2nd order spherical harmonic) were performed for a slightly larger volume than the one covered by the full-FOV EPI sequence (Table 1, protocol A). The shim coil currents for minimizing static field variations were calculated with the default algorithm provided by the vendor. The outer volume suppression allowed for the slices to be oriented parallel to the long axis of the calcarine sulcus (i.e., oblique axial), which provided high-resolution imaging of the primary visual cortex (V1) without requiring an extended EPI echo train length (ETL) or compromising SNR due to g-factor losses associated with high parallel imaging acceleration. However, the increased power deposition caused by the outer volume suppression pulse, limited the number of slices to 17 for TR of 2 s. In order to obtain comparable steady state magnetization levels and sensitivities to physiological signal variations, this TR was used in all EPI measurements. In addition, an increased GRAPPA acceleration factor was used for the full-FOV measurements (protocol A) which permitted to keep the echo train length in a similar range as the one of the zoomed protocol with a voxel size of 650 μm. The ordering of the EPI protocols was pseudo-randomized for each subject, and each fMRI scan was proceeded by the corresponding PSF-mapping scan.

Visual stimuli were presented to the subjects on a screen viewed through a mirror mounted to the inside of the RF coil housing, and consisted of an initial 30 s rest period followed by 16 trials with 10 s stimulation (9° visual field radial checkerboard, 8 Hz flickering rate) and 24.5 s rest, before a final 30 s rest period. Thus, 306 volumes were acquired for each run and protocol (TA approx. 11 min including GRAPPA reference line scan). The duration of the rest periods was not a multiple of TR, which provided a successive shift of the stimulus onsets by 0.5 s to obtain a higher effective temporal resolution of the BOLD responses. In order to ensure the subjects' attention to the stimulus, participants were asked to fixate a target point (subtending 0.2° of the visual field) at the center of the screen and to confirm its randomly appearing color change (red-orange, every 8–30 s, duration 0.5 s) by pressing a button on a feedback device. The subjects' performance was recorded and presented at the end of each run to provide feedback. Over the course of the entire study, a single run, where the behavioral data showed a substantial drop in the volunteer's attention (more than three false or excessively delayed responses), was repeated.

2.1.3. Anatomical measurements

As anatomical reference, a 0.4 mm isotropic T_2*-weighted 3D FLASH image, with the same oblique orientation as the EPIs, and a 0.6 mm isotropic, transversally oriented MP2RAGE (Marques et al., 2010) were acquired at the end of the sessions. The gradient-echo parameters were as follows: TE = 16 ms, TR = 29 ms, FA = 12°, BW = 141 Hz/pixel, GRAPPA = 3, 6/8 partial Fourier, matrix size = 480 × 480 × 88, TA = 6:30 min. For the MP2RAGE sequence, a 13 ms long, non-selective TR-FOCI inversion pulse (Hurley et al., 2010) was used. Other parameters: TR = 6 s, echo spacing = 6 ms, TE = 3 ms, $FA_{1/2}$ = 5°/9°, $TI_{1/2}$ = 800/2000 ms, GRAPPA 2 × 2 (CAIPIRINHA k-space shift = 1 (Breuer et al., 2005)), 6/8 partial Fourier in secondary phase encoding direction, matrix size = 352 × 352 × 256, TA = 10:48 min.

2.1.4. Image reconstruction

Images were reconstructed offline with in-house-developed Matlab (The MathWorks, USA) routines. The EPI reconstruction consisted of ramp sampling regridding, correction of dynamic B_0 changes (DORK (Pfeuffer et al., 2002a)), navigator-based Nyquist ghost correction, as well as GRAPPA reconstruction and a projection onto convex sets (POCS (Haacke et al., 1991)) in order to recover the skipped lines due to parallel imaging and partial Fourier acquisition, respectively. GRAPPA and POCS were only utilized for the reconstruction of the anatomical data. Combination of the signal of the individual coil elements was achieved with the adaptive

Table 1
EPI sequence parameters.

protocol	FOV [mm] (read x phase)	matrix	voxel size	accel. factor/no. of reference lines	BW/px [Hz] [a] BW/mm [Hz] [b]	ETL [ms]	PSF scan parameters	
							duration [min:ss]	rFOV factor [c]/encoding steps
A	180 × 180	224 × 224	800 μm isotropic	4/88	1174 21.5	44.1	2:14	4/56
B	150 × 106	188 × 132	800 μm isotropic	3/66	1156 27.3	34.7	2:32	2/66
C	150 × 66	230 × 102	650 μm isotropic	2/40	1144 26.0	44.1	2:00	2/52

where: Δt_y = nominal echo spacing as given by the scanner/parallel imaging factor.
FOV_y = FOV in phase encoding direction.
Consistent for all protocols: TE = 26 ms, nominal FA = 70°, 17 slices, TR 2000 ms, 6/8 partial Fourier.
[a] Bandwidth in readout direction as given by the scanner.
[b] BW/mm (in phase encoding direction) = $1/(\Delta t_y \cdot FOV_y)$.
[c] reduced FOV factor in PSF encoding direction. See (Zaitsev et al., 2004) for details.

combine method (Walsh et al., 2000) in all sequences. For the zoomed EPI, only coil elements located in the posterior part of the head were used for reconstruction. From the PSF pre-scan, the magnitude distortion correction kernel, a voxel-shiftmap, a distorted (i.e. EPI like) and a distortion free (i.e. GE-like) reference image were derived (Zaitsev et al., 2004). The EPI-like image is the projection along the EPI phase encoding direction and the GE-like image the projection in the additional PSF encoding direction, respectively. The geometric distortions in the time-series EPI data were corrected using two different PSF methods: either by applying the voxel-shiftmap using cubic interpolation ('PSF shiftmap') (Chung et al., 2011) or by performing a local interpolation with the weights of the magnitude PSF kernel in order to derive the voxel value in the distortion corrected space ('PSF kernel') (In and Speck, 2012).

In order to minimize any residual bias provoked by the strong transmit field inhomogeneities at 9.4 T, the MP2RAGE contrast as well as the associated T_1-map were calculated with retrospective B_1^+-inhomogeneity correction (Haast et al., 2018; Hagberg et al., 2016). This was achieved by first co-registering the AFI data to the second image contrast generated by the MP2RAGE (corresponding to TI_2). Then, a quantitative T_1 map was derived from a look-up table by taking the measured MP2RAGE signal intensity and the achieved flip angle. Finally, the B_1^+ corrected T_1 map was utilized to obtain the MP2RAGE contrast with the nominal flip-angles of the sequence. For the automatic detection of large veins, a susceptibility weighted image (SWI) was calculated from the anatomical FLASH dataset using a sigmoid phase mask (Martinez Santiesteban et al., 2006). On this SWI, a vessel filter function was applied (Frangi et al., 1998). The parameters of the Matlab implementation of the filter (Kroon, 2009) were adjusted manually, based on visual inspection of the accuracy and robustness of the venous detection ($\alpha = 0.1$; $\beta = 0.5$; $\sigma = 0.1$–1.2, $\Delta\sigma = 0.1$; $C = 0.02$). For all other ('non-venous') voxels, the 3D Euclidian distance to the nearest segmented vein was calculated.

2.2. Postprocessing

2.2.1. Performance of prospective motion correction

The amount of retrospectively detectable subject motion despite the PMC was determined with SPM 12 with respect to the first volume of each time-series. For the comparison of the PMC recorded subject motion with the estimated residual motion, the tracking data was averaged for the 17 slices of each volume. With the translations (in mm) and rotations (in degrees) of a unit sphere, the total displacement of the individual volumes (i) with respect to the first volume was calculated as:

$$D_i = \sqrt{x_i^2 + y_i^2 + z_i^2 + P_i^2 + R_i^2 + Y_i^2}$$

where x, y and z represents translations in the x, y, and z-direction, respectively, P represents pitch-rotation, R represents roll-rotation, and Y represents yaw-rotation.

This equation was adapted from (Todd et al., 2015) and allows the comparison of relative displacements between individual measurements. Using the same weights for translations and rotations corresponds to displacements as they would have occurred on a sphere with a radius of 57 mm, which is a good approximation of the size of a human head. In order to estimate the magnitude of the scale of intra-volume motion, we also extracted the maximum and mean values of the translational and rotational components during the acquisition of the 17 slices of each image volume.

It is well-known that retrospective motion correction introduces spatial blurring due to the required image resampling (Polimeni et al., 2018). The additional blurring that would have been induced in our data by retrospective motion correction was simulated using the camera recordings provided of the optical tracking system for three representative cases of small, medium and large motion patterns. For this simulation, the image resampling was performed with 5th order spline interpolation. The Supplementary Material contains details about the simulation, the impact of the resampling interpolation method, and the representative motion time-courses. We also estimated the accuracy of the residual motion estimation for images with similar FOV and SNR as the ones acquired in this study.

2.2.2. Calculation of cortical depths

The T_1-weighted MP2RAGE images were first segmented with the MIPAV algorithms implemented in CBS tools (Bazin et al., 2014), followed by splitting the segmented cortex into five level sets using the equi-volume principle (Waehnert et al., 2014). Since data was analyzed in EPI space, the required spatial transformation was derived by first registering the FLASH-like reconstruction of the corresponding PSF pre-scan to the 3D-FLASH image, then registering the 3D FLASH image to the magnitude of the second contrast image of the MP2RAGE measurement. Afterwards, the two transforms were combined and the level sets derived in anatomical space were resampled into functional space using 5th order spline interpolation. Using level sets for the spatial transformation instead of discrete voxel labels has the benefit that the equi-volume condition remains fulfilled in the distorted space. All image registration and resampling were performed using SPM 12. Based on these level sets, five sub-volumes, which we will refer to 'depths' in the following, were computed. Taking the outermost and innermost level sets, respectively, we also formed a pial ('CSF') and a subcortical ('WM') depth outside the cortical gray matter boundaries defined as those EPI voxels within a distance of 0.5 mm to the nearest GM level set. The depths in the native/distorted functional space were obtained by warping each level set with the inverse of the PSF shift map before discretizing the depths.

2.2.3. Effects of local distortions on depth identification

The effect of susceptibility differences between venous blood and the surrounding tissue on the spatial accuracy of distortion correction, was investigated by evaluating voxel-shifts obtained from a 650 μm isotropic PSF scan along a path cutting through the folding pattern of the cortex and crossing several large veins. Here, the PSF shifts were considered as the ground truth since they yielded an accurate match of the distortion corrected EPI to the corresponding anatomical images (see Fig. 4 a, b). For comparison with the standard method for dewarping images at lower resolution/field strengths (Jezzard and Balaban, 1995), the corresponding voxel displacements were obtained from a standard B_0 measurement with 2 mm isotropic resolution ('B_0-shiftmap'). In contrast to the already aligned PSF shifts, the B_0-shiftmap displacements required an additional registration step to the distortion-free reference of the PSF scan. Since subject motion between the distortion mapping scan and the functional scan can also decrease the accuracy of distortion correction, we artificially moved the PSF voxel-shifts by the maximum recorded motion between the reference and the functional scan of all 12 runs, denoted as 'PSF*-shift map' in the following (with x-, y-, z-translation: 0.2 mm, 0.36 mm, 1.5 mm; pitch-, roll-, yaw-rotation: 0.67°, 0.48°, 0.18°). Assuming that the PSF shift map represents the ground truth of the geometric distortions, the spatial origin of the signal measured at the locations with the largest local displacement was also estimated.

2.2.4. Blurring induced by distortion correction

Image interpolation causes spatial blurring if the voxel displacement required for distortion correction leads to a shift that places the voxel between grid points of the voxel grid. The extents of blurring induced by the distortion correction with the PSF kernel, the PSF shift map, and the shifts derived from a B_0 mapping scan were estimated using the methods described previously ((Renvall et al., 2016), in their Supplementary Material). A simple 1D cubic interpolation was used for the distortion correction for the latter two methods. We also estimated this blurring effect using an alternative approach based on calculating how the signal of a single cortical depth would be distributed to the adjacent voxels after dewarping. This was performed by first creating a binary mask for the

voxels belonging to the central depth in the native/distorted space, and then applying the resampling (5th order spline).

2.2.5. Influence of large veins on cortical depth BOLD profiles

As with other methods of performing functional signal extraction in laminar fMRI, the NIPYPE (Gorgolewski et al., 2011) workflows used in this study were designed to minimize the amount of resampling of the functional EPI data. First, using prospective motion correction avoided any resampling for motion correction. Second, the PSF shift map was used for distortion correction to ensure high spatial accuracy. To test whether the results are affected by the functional data interpolation due to the dewarping, the signal extraction was performed in the native (distorted) EPI space as well. In other words, one pipeline allowed the signal extraction in the anatomical space, but required distortion correction of the functional data. The other one used the distorted level sets of the cortical depth segmentation and vessel distances to perform signal extraction in the native EPI space. The data workflow is depicted in the Supplementary Material (Figure A9) and is briefly described below for the distortion corrected data processing case:

1. A standard GLM analysis was performed for the slice timing corrected and high pass filtered (cutoff 90 s) functional data using a filtered canonical hemodynamic response function (HRF). The obtained z-score maps were resampled into the anatomical space of the SWI volume (400 μm resolution) and thresholded at $z > 2.3$ (uncorrected). Then, the masks of the BOLD activation data from the different protocols (A-C) were combined using a binary operation such that only areas showing statistically significant signal changes during all three runs were considered for further processing. These masks were then extended along the cortical normal vector if at least 40% of the voxels along the normal were labeled "active" in the previous step. The created mask was then resampled back into the individual functional spaces using nearest neighbor interpolation and thresholded at 0.5. This procedure allowed for an evaluation of signal changes sourcing from the same ROI for all protocols independent of spatial resolution and coverage.

2. The signal time courses of the individual voxels classified as "active" were extracted from the low-pass-filtered and slice-timing-corrected data. For each of these voxels, we also determined the corresponding depth (one of the 7 defined depths, i.e., CSF, gray matter depth 1–5, or WM) and the Euclidian distance to the closest vein detected by the vessel segmentation (0–2.5 mm, binned step width = 0.5 mm). Voxels with a negative shift (stretching) of more than 0.5 voxels during the distortion correction step had a true resolution that was much coarser than the nominal image resolution; this loss in resolution cannot be recovered, thus these voxels were omitted from further analysis.

3. The functional data within each ROI were normalized to the mean of the baseline periods at the beginning and end of each run. After low-pass filtering with a cutoff frequency $f_{cutoff} = 0.3$ Hz, the data of periods with similar stimulus onsets were pooled and reordered depending on the actual stimulus onset time, resulting in HRF time-courses with 0.5 s temporal resolution.

Then, the voxels were sorted according to their 3D Euclidian distance from the closest identified vein and their cortical depth. Sets of voxels were only considered if the number of significant voxels was equal or greater than to 50 at 800 μm, or 93 at 650 μm resolution, respectively. This arbitrary thresholds ensured that the minimum cluster volume was equivalent for the two resolutions (approximately 25.6 μl). The additional temporal low-pass filter enabled the reliable determination of the peak signal amplitude of each individual response (different Euclidian distance bin and different depth bin) and was assumed to have negligible effects on the overall outcome due to the slow dynamics of the BOLD response.

3. Results

3.1. Performance of prospective motion correction

Fig. 1a depicts the camera based prospective motion tracking data from an example run with 800 μm resolution. The high accuracy of the PMC allowed to detect even small movements, for example due to breathing (Fig. 1b), which typically results in within-volume movements due to their rather high frequency. The image based retrospectively estimated residual motion parameters indicate that the PMC was able to correct for the small drift-like motion as well as a rapid displacement (Fig. 1c, gray shaded area). This can be also seen in Fig. 1d which shows images of one slice acquired before and during the largest motion in this run.

For all subjects, the most dominant types of motion were translations in *z*-direction (along the scanner axis) and nodding-like rotations. In most cases, the prospectively corrected subject motion was larger than the retrospectively estimated residual displacements which lead in addition to more comparable residual motion across the individual subjects and runs (Fig. 2, Supplementary Figure A1a and A1b for results of individual runs). Thus, the mean displacement with respect to the first volume of each run decreased from 0.55 ± 0.37 to 0.23 ± 0.14 mm. This corresponds to a reduction of the mean translations in mm and rotations in degrees from 0.225 to 0.094. The mean within-volume translation and rotation amounted to only 0.073 mm and 0.035°, respectively. However the maximum displacement during the acquisition of a single volume amounted to 1.86 mm and 0.52° (Fig. 1). The mean and maximum position change between the PSF reference scan and the corresponding functional scans were measured as 0.18 mm/0.17° (D = 0.46 mm) and 1.5 mm/0.78° (D = 1.94 mm), respectively. Despite the different motion characteristics, the estimated mean blurring, which would have been introduced in case of retrospective motion correction, yielded a median FWHM of a comparable Gaussian kernel width of 0.78, 0.86, 0.85 mm for the 'small', 'medium 'and 'large' motion cases, respectively for a 1 mm voxel grid (see Supplementary Material for details).

3.1.1. Effects of local distortions on depth identification

The spatial distortions measured with the PSF scan in one of the four subjects are depicted in Fig. 3a. Since the displacement expressed in millimeters scales with the total readout duration and spatial resolution, the distortions of the 650 μm data (protocol C) are at the same scale as the distortions of the 800 μm measurement with shorter ETL (protocol B), while much stronger distortions are visible in the full FOV measurement. Independent of the resulting voxel shifts in phase encoding direction, the PSF method was able to map and correct the distorted images with high precision (Fig. 3b). As expected, the higher spatial resolution allows to better differentiate anatomical details, as can be seen in the single frame 650 μm and the 800 μm images before and after PSF kernel distortion correction (Fig. 3c).

The spatial displacements derived from a PSF reference scan with 650 μm resolution and a co-registered 2 mm isotropic B_0-map were found to be of comparable magnitude for voxels distant from large veins (Fig. 4 a – d). Close to large veins (dark blue lines), however, large deviations between the calculated voxel shifts from the PSF and B_0 mapped of −1.5 to +2.5 mm occurred in this example. The shifts along the phase encoding direction either in positive (at ① and ③ in Fig. 4 b and d) or negative direction (at ②) were likely caused by the dipole like static field variations around large veins which can result in positive and negative static field offsets. In the uncorrected data, there is also tissue signal smeared into large veins (arrow in 4a). The strongest difference in local distortion between the correction with the PSF shift map and the B_0-shiftmap of approximately 2.2 mm can be seen in a region where no vein was directly visible in the EPI and SWI (label ②). The calculated displacements of voxels show that the local field perturbations actually lead to a mixing of signal originating from tissue and large veins. This effect is visualized by the light blue lines which represent the origin of the voxels at point 1–3 in the distortion corrected space. The observed effect may therefore result in venous signal contributions in cortical voxels.

3.1.2. Blurring induced by distortion correction

Although image distortions were successfully corrected by the

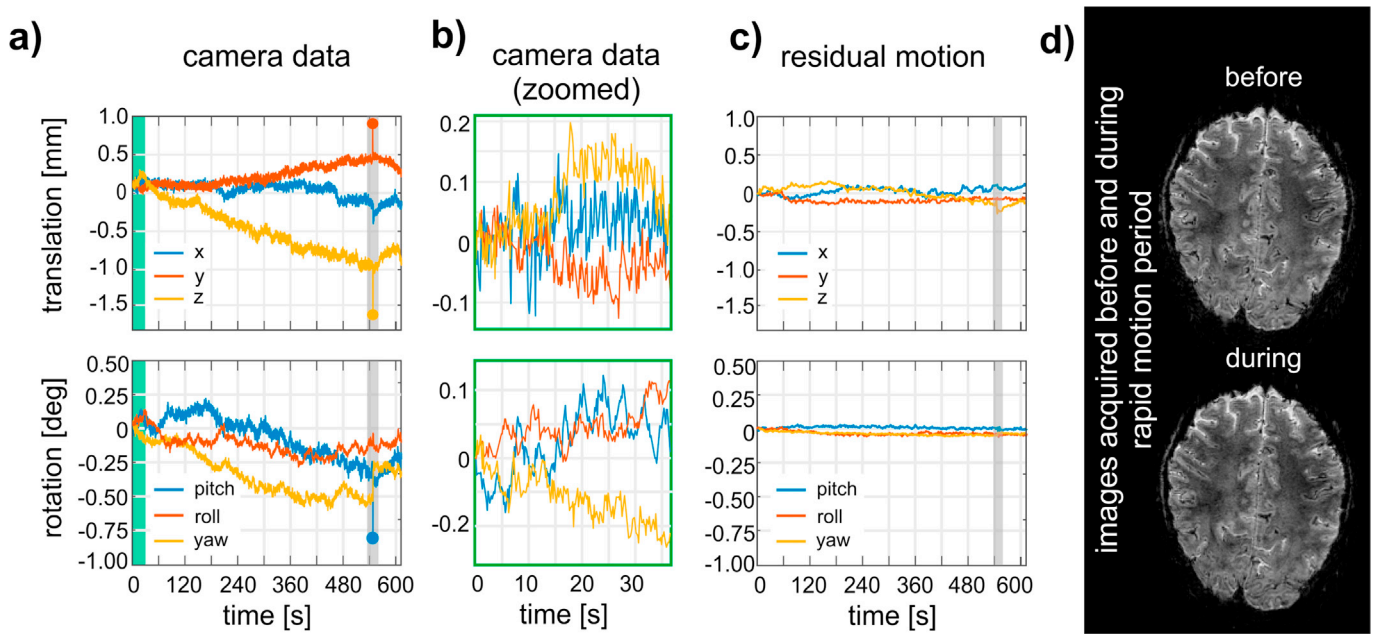

Fig. 1. Motion recorded by the PMC system, residual image motion and image quality during rapid motion period. Head displacements recorded during one run with 800 μm isotropic resolution (a). The high sampling rate and resolution of the PMC system is visible in the zoomed view of the green period in (b), where motion due to breathing can be observed as repetitive rotations around the pitch axis. The graph in (c) shows the residual motion estimated by retrospectively aligning the images of the same run. Even the single rapid displacement during the measurement (marked points inside gray shaded areas in (a) and (c)) was corrected successfully, as can be seen in the almost identical images acquired before and during this rapid motion (d).

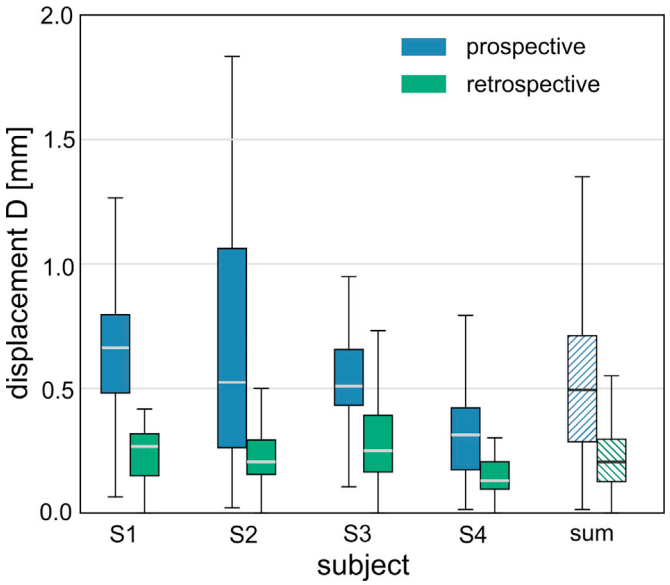

Fig. 2. Comparison of corrected displacements (blue) and estimated residual motion (green) for all subjects and runs. The boxes indicate the 25 and 75% quantiles and the whiskers the total motion range. One can also see that the PMC helped to reduce differences in motion across subjects resulting in more similar distributions of retrospective displacement estimates than for the camera recorded displacements.

magnitude PSF kernel interpolation approach, the method induced stronger image blurring than the simple image warping using the PSF shift map or the voxel displacements derived from the B_0 mapping. Consequently, these blurring effects were also visible in the activation maps (Fig. 5b) as an increased number of voxels exceeding the chosen significance threshold of $z > 2.3$, since the image blurring degraded the effective spatial resolution and caused signal averaging, thus increasing tSNR. After distortion correction with the PSF kernel method, the number of voxels above the z-score threshold were on average 3.6%, 5.2% and 7.2% higher for protocols A, B and C, respectively, than without any distortion correction. The impact of distortion correction on the activation detection sensitivity was thus highest for the protocol with the lowest tSNR and did not scale with the degree of the distortions. The simulated impact on the depth analysis is shown in Fig. 5c, where the signal is seen clearly to spread from the central depth to neighboring voxels in case of PSF kernel correction, whereas the PSF shift map correction only leads to minor signal spread. The images depicted in Figs. 4 and 5 are based on the calculations performed on a dataset acquired with imaging protocol C (650 μm resolution), but the results for the other sequence protocols were comparable (Supplementary Material Figure A6).

3.1.3. *Influence of large veins on cortical depth BOLD profiles*

The variation in temporal SNR of the different fMRI protocols (Supplementary Material Figure A7) resulted in 36.3% more voxels having a z-score>2.3 in the 800 μm full FOV (protocol A) versus the 800 μm zoomed measurements (protocol B). Similarly, the volume of voxels which exceeded the significance threshold was 11.3% higher in 800 μm zoomed data compared to the one acquired with 650 μm isotropic resolution (protocol C) despite the large difference in voxel volume and the corresponding difference in image SNR. However, the formation of the activation ROI accounted for the differences in resolutions across protocols. Since the outcomes from the HRF analysis performed in anatomical space and the native EPI space were nearly identical, we will focus on the results obtained using the distortion corrected images in the following. The venous network in the volume covered by the 0.8 mm full FOV functional measurement is visualized in the minimum intensity projection of the SWI in Fig. 6a. Fig. 6b depicts enlarged views of ROIs located in the prefrontal cortex and the visual cortex, respectively. Despite the resolution of 400 μm isotropic, ascending veins are only visible in the prefrontal cortex (indicated with small arrows). The anatomical relationship of large veins and the cortex becomes clear in the overlay of the calculated Euclidian distances of the automatically segmented veins on the central slice (Fig. 6c) which shows that most

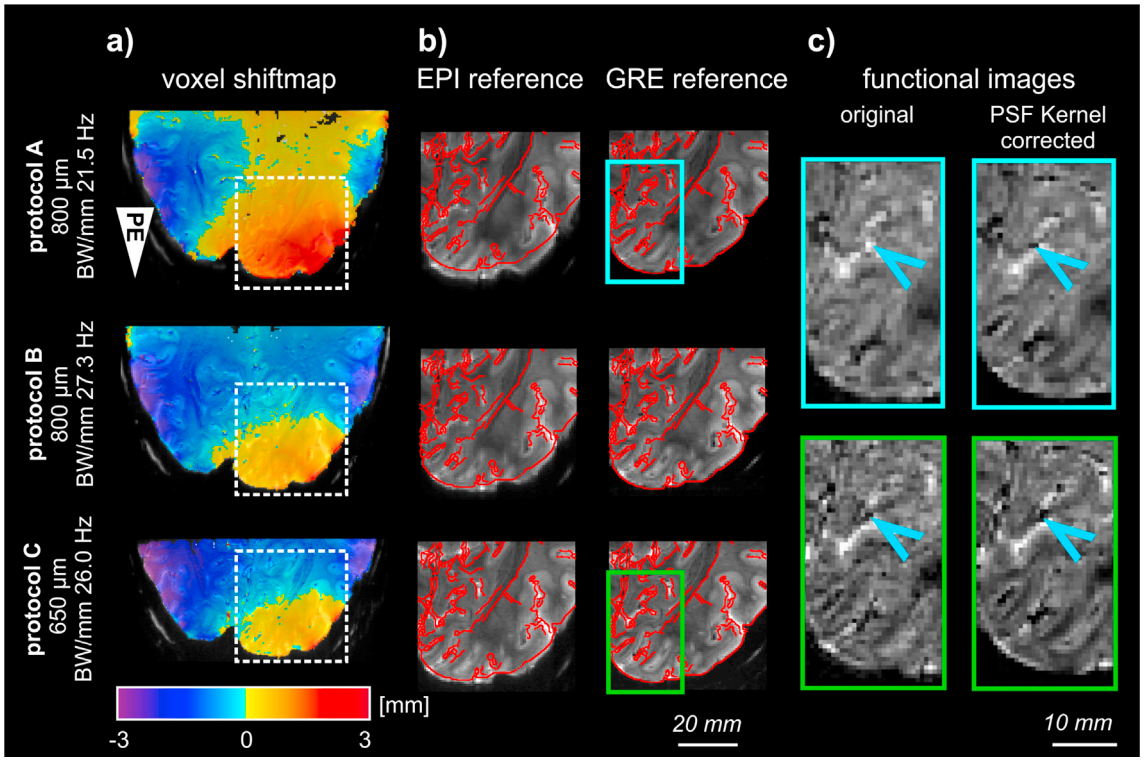

Fig. 3. Impact of phase encoding bandwidth on geometric distortions, and the accuracy of PSF-based distortion mapping. (a) The degree of spatial deformation scales with the BW/mm, thus, similar distortions can be observed in the measurements with protocol B & C despite the different resolution and ETL. The phase encoding direction (posterior → anterior) is indicated by a white arrow. (b) Overlay of contours derived from the high-resolution 3D FLASH on the EPI-like and GE-like reconstruction obtained from the PSF reference scan (For details, see (Zaitsev et al., 2004)). (c) Example single frame images of functional images acquired with protocol A (top) and C (bottom). Note the improved visibility of large veins in the distortion corrected data for example at the blue arrow.

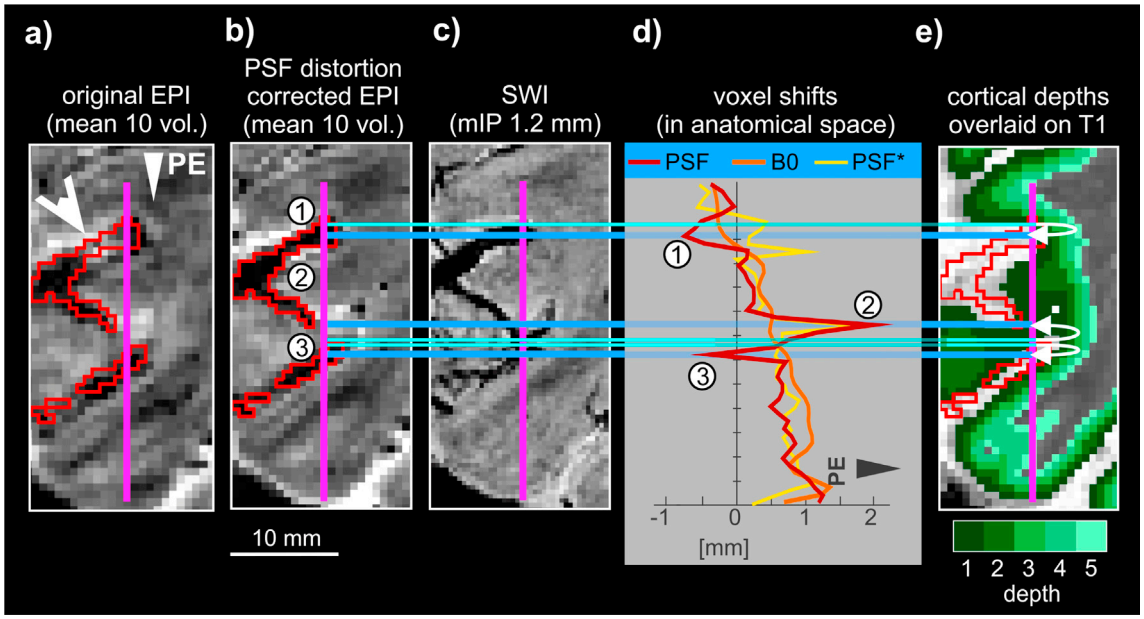

Fig. 4. Geometric distortions near large veins. As an example, displacements of voxels along the pink line depicted in (a) – (c) are shown in (d) for the PSF shift map (PSF), the shifts derived from the 2 mm B_0 map and the simulated motion between the distortion correction and the functional measurement (PSF*). Strong static field perturbations near large veins (indicated by the thick blue lines and the white arrow in a)) were only captured by the high resolution PSF scan (label ① – ③). Signal observed at the thick blue lines after distortion correction actually contains contributions from areas at the light blue lines, too. Also note the difficulty of identifying large veins (red contours) in the T_1 image due to similar relaxation times as GM.

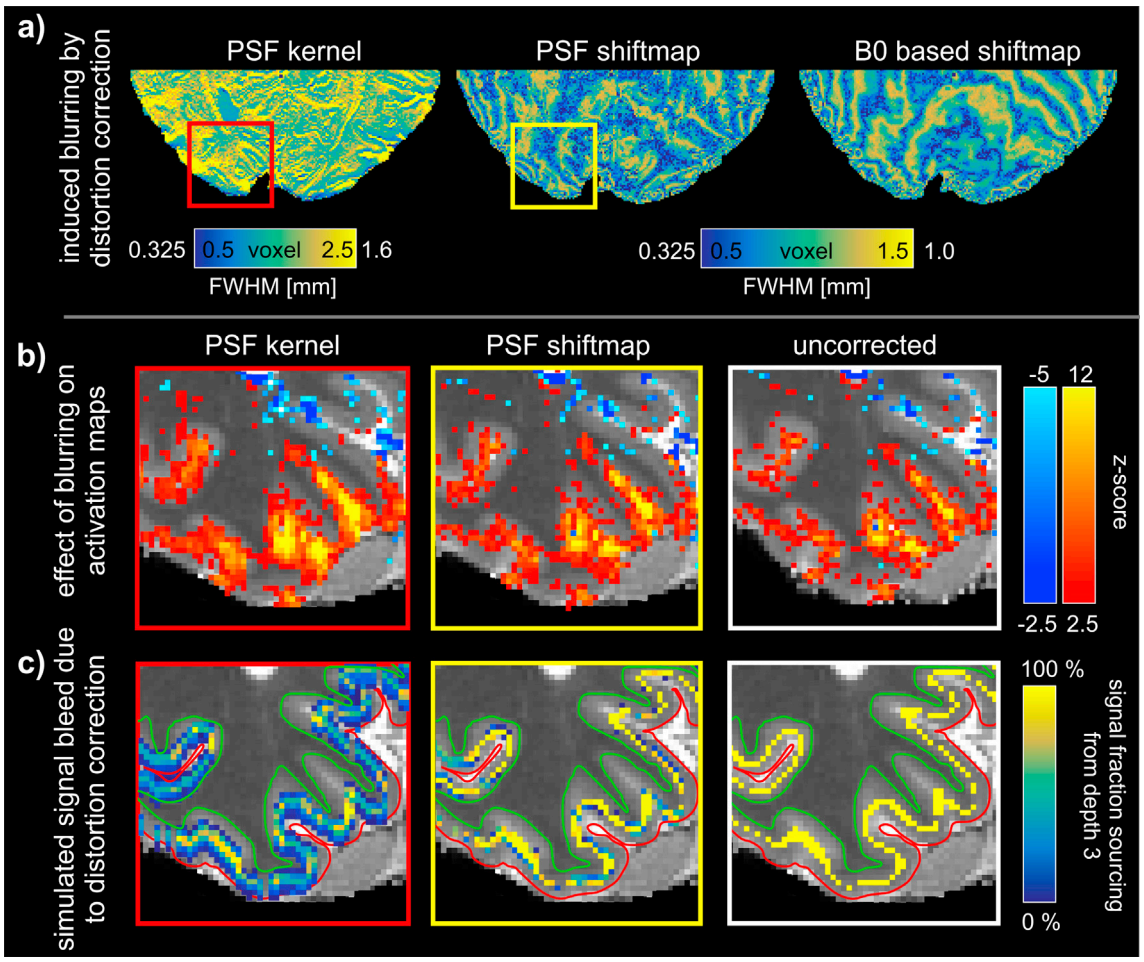

Fig. 5. Simulated blurring provoked by different distortion correction techniques. The PSF kernel correction caused strong signal spreading independent of the amount of voxel displacement. In contrast, the PSF shift map and the B_0-based shift map blurring are almost similar (a). Please note the different scaling of the kernel and the shift map corrected images, respectively. (b): The stronger blurring of the PSF kernel method is also apparent in GLM results leading to an increased number of voxels with $|z|>2.5$. Thus, in case of a laminar analysis, strong blurring could prevent correct differentiation of signal originating from different depths (c).

large veins, beside the deep medullary veins, are located in proximity to cortical gray matter or even appear to intersect gray matter (inserts in Fig. 6c). The ability of the filter function to detect veins is in addition visualized in the Supplementary Figure A8. In the volume covered by the SWI, 59% of the voxels in the cortex were closer than 1.5 mm to the nearest identified vein (Fig. 6d left). If the same calculation was performed for the voxels considered for the evaluation of the BOLD time courses, this value increased to 75% (Fig. 6d right). However, the distribution with the individual cortical depths was almost identical.

The plots in Fig. 7a show the BOLD amplitude across cortical depths after normalization for the mean amplitude in gray matter (depth 1–5) for each subject. For all protocols the functional response amplitude increased towards the cortical surface. The strongest signal gradient can be observed in the measurements performed with protocol C, however, there is only little variation of BOLD signal increase across subjects. The data of an example subject (S2) in Fig. 7b shows that the functional responses have comparable shapes across cortical depths except for a higher amplitude in the 650 μm measurement compared to 800 μm data. All responses show an increase of signal amplitude and duration of the positive response towards the cortical surface.

A more distinct behavior can be seen in the analysis of the BOLD responses sorted as a function of distance to the closest segmented large vein (Fig. 8a). The signal change is strongest close to large veins and declines with increasing distance. Independent of the distance to large veins, an increase in signal amplitude towards the cortical surface can be observed whereas the post-stimulus undershoot appears to be mainly dependent on the distance to the segmented veins. In order to test for the influence of higher blood volume in the more superficial depths, the BOLD responses were re-sorted by the cortical depths and plotted as a function of Euclidian distance in Fig. 8b. There, a higher BOLD response near veins becomes visible even for depth 3.

The gradient of the BOLD amplitude increase towards the cortical surface is dependent on the vessel distance for the other protocols as well (Fig. 9a). For example, in the topmost cortical ROI (depth 1) measured with protocol B, the signal near veins (0–0.5 mm) was about 68% higher than the mean signal amplitude in this depth and 2.15 times higher than signal sampled at 1–1.5 mm from veins in the same depth. The depicted response amplitudes were normalized by the mean response amplitude in the cortex for each subject before averaging. Fig. 9b illustrates the response amplitude for different cortical depths as a function of Euclidian vessel distance (as illustrated in Fig. 8b). The data depicted in this plots were normalized by the peak response amplitude in each depth and averaged across subjects. One can see that the dependency of the relative signal amplitude on the venous distance varies only slightly for CSF and cortical depths 1–4. Please note that only datasets in which the number of voxels in the ROI was larger than 50 were considered in the analysis. For small vessel distances this was only achieved for CSF and depths 1–3, which can be explained by the fact that voxels located at deeper cortical locations had a higher vessel distance per se (cf. Fig. 6b). Fig. 9 shows results obtained in the anatomical (distortion corrected EPI space). Similar behavior can be seen by plotting BOLD signal amplitudes extracted in native (distorted) EPI space (Supplementary Material Figu.

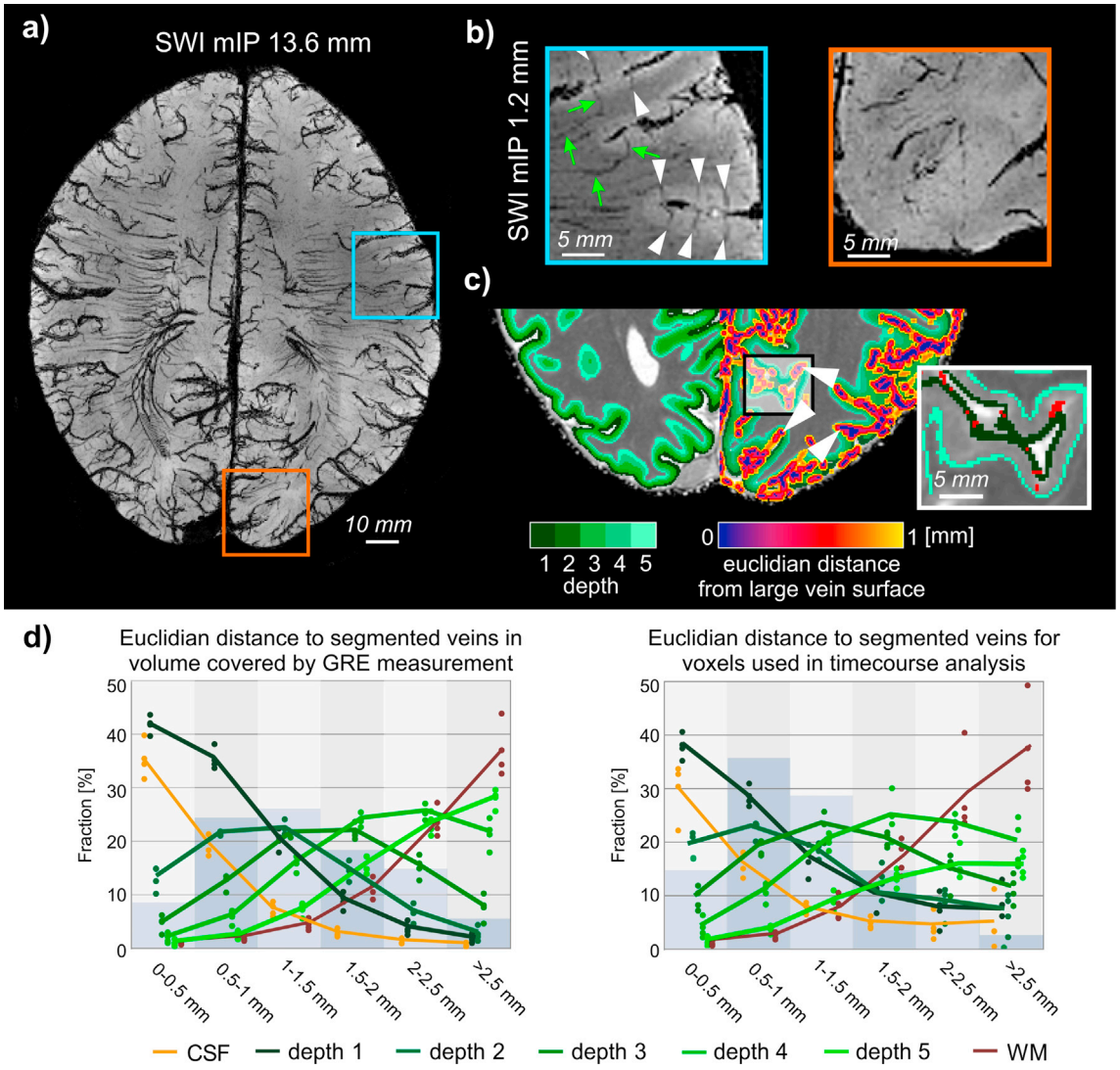

Fig. 6. SWI contrast and impact of applied activation masks on distributions of voxels. Minimum intensity projection across the full volume of an 800 μm measurement (a). Ascending intracortical veins are not visible in the primary visual cortex (orange box in (b)) but are visible in other cortical areas (blue box). In (b), green arrows indicate vessels originating from white matter which are likely principle cortical veins and white arrows point to apparent ascending veins. The large veins considered for the analysis are predominantly located near gray matter in the subarachnoid space between dura mater and the cerebral cortex or in sulci (c). However, there are also large veins apparently intersecting gray matter (indicated with arrows and enlarged for an example region in the insert). The histograms in (d) show the overall fraction of cortical voxels within a certain distance to the nearest segmented vein as vertical bars. The left plot depicts results for the complete volume covered by the high-resolution 3D FLASH measurement and the right plot for voxels considered in the BOLD response analysis. The colored lines represent the individual depths (normalized for each Euclidian distance) and the points the values from the individual subjects.

A10). Note that in this case a sufficient number of voxels exceeding the significance threshold in at least three subjects was only achieved for vessel distances smaller than 2 mm.

Overall, two major aspects can be observed: First, the signal decay with increasing vessel distances is almost identical for the different protocols (especially near the cortical surface). Second, voxels with vessel distances $\geq$1 mm had only approximately 60% of the signal amplitude of the voxels less than 0.5 mm from a vein, confirming the strong dependency of the GE-BOLD amplitude on large vessel distance. For Euclidian vessel distances above 1 mm, the influence of large veins declines rapidly. The corresponding linear fit results of the BOLD amplitude increase towards the surface for the different vessel distances and protocols are listed in Table 2.

4. Discussion

In this study we used several methods which are expected to allow for spatially accurate fMRI data, including increased resolution, precise geometric distortion correction as well as camera-based motion correction and registration. In addition, the characterization and removal of biases through explicit segmentation of large cortical veins was performed for task provoked BOLD signal changes.

4.1. Prospective motion correction in laminar fMRI

In order to accurately compare across subjects and sequences, the motion correction method should be independent of image contrast, quality and motion characteristics. We observed in the recorded head positions that intra-volume motion is a minor problem for laminar fMRI studies because of its small amplitude. Nevertheless, rapid or within-volume movements will still reduce data quality and may be missed by retrospective motion correction. However, if large changes in head motion can be robustly identified, the data corresponding to these corrupted volumes can be discarded to reduce errors in the final fMRI analysis. A strong influence of motion correction performance on the accuracy of laminar analysis results can also be expected in cases of subject motion

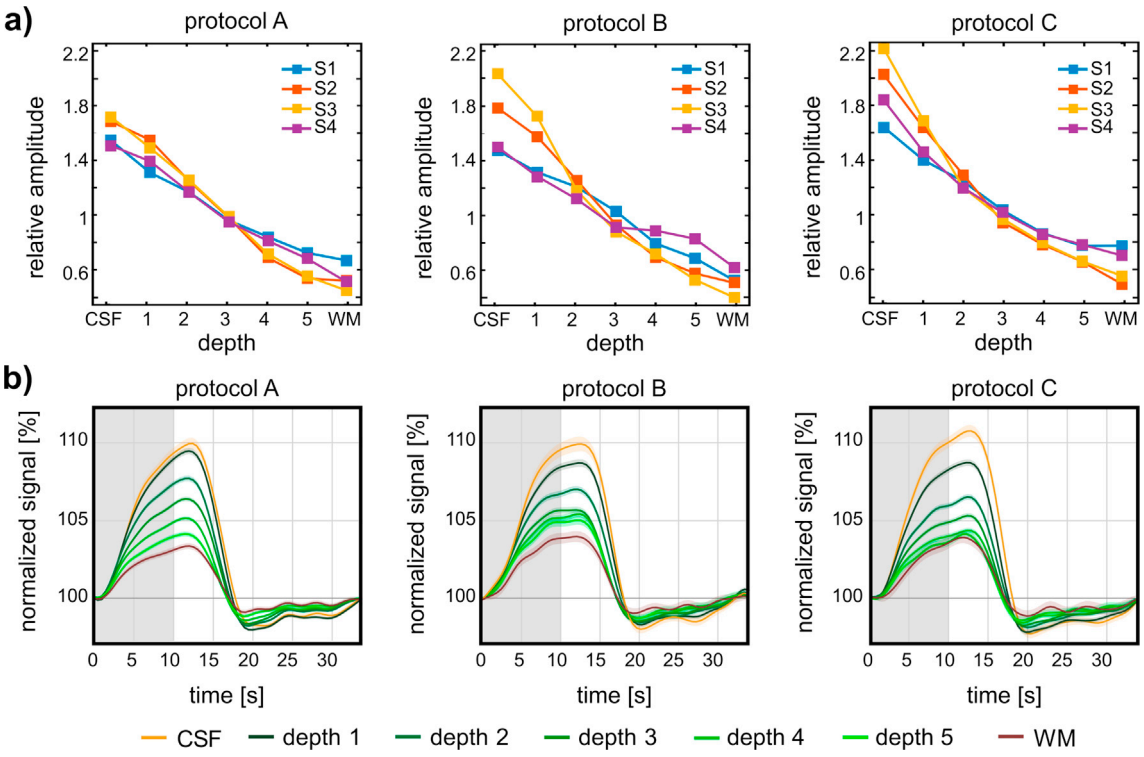

Fig. 7. Depth dependency of peak BOLD amplitude for different subjects (S1–S4) and protocols). For a better comparison across subjects the values in (a) were normalized for each subject such that the mean baseline amplitude over the cortex equals one. All protocols and subjects show an increasing signal towards the cortical surface. (b) BOLD responses from an example subject (S2) and all three protocols. The plots illustrate that the signal continuous to rise after the end of the stimulation period (gray shaded area) and the signal amplitude increases towards the pial surface. Furthermore, larger depths appear to have a shorter response duration. Interestingly, the amplitude of the post-stimulus undershoot is almost identical independent of the cortical depth.

between the distortion mapping and the actual functional measurements. Even if this inter-scan motion is corrected, one should be aware that variations in head position may alter the B_0 field, too, which can result in variations in image distortions (Jezzard and Clare, 1999). This issue also affects processing strategies which are based on the acquisition of anatomical data in the distorted space and can possibly only be avoided by incorporating dynamic distortion correction techniques (Dymerska et al., 2018).

In this study, a quantitative comparison of prospective and retrospective motion correction was omitted. Such experiments require comparable motion patterns across different runs and independency from any other sources of image displacements such as spurious shifts in phase encoding direction in case of insufficient correction of dynamic off resonances variations (Pfeuffer et al., 2002a) or variations in image distortions during head motion (Jezzard and Clare, 1999). Instead, retrospective motion correction, which is the standard in fMRI post-processing, was used here in order to estimate the residual motion in the image data. Yet, the observed remaining displacements despite PMC were larger than the nominal accuracy of the PMC (see Methods section) and the recorded marker position variation during an EPI phantom experiment (standard deviation of marker position 0.016 mm/0.008°). Since the retrospectively estimated displacements were also larger than the estimated accuracy of the retrospective motion correction (Supplementary Figure A5), it can be assumed, that the detected residual motion was provoked by the previously mentioned sources and may therefore only be reduced by combining PMC with dynamic distortion correction, as proposed by others (Ooi et al., 2013).

Complementing a recent study (Polimeni et al., 2018), we observed that the mean blurring induced by retrospective motion correction would have led to an almost homogenous reduction of spatial resolution for the simulated motion patterns. Although single movements caused distinct smoothing patterns, these patterns are averaged out during the full time-course in the typical case of drift-like motion (see Figure A3 in Supplementary Material). Hence, if other effects like potential changes in image distortions and spin-history effects are ignored, the overall impact of retrospective motion correction on the spatial accuracy can be expected to not be dominated by the maximum magnitude of displacement. Instead, even smallest displacements already lead to a reduction of spatial accuracy due to image resampling. The resolution losses during retrospective motion correction can however be reduced by first up-sampling the data to a finer image grid before applying the motion transform. The main obstacle of using the chosen PMC method is the need to produce individual occlusal splints for each subject to ensure proper tracking of the subjects head and a direct line-of-sight of the camera on the marker in case of a closed head coil housing. This time consuming manufacturing and fitting process limited the number of subjects to four but may be improved in the future due to latest developments in digital intraoral impressions and 3D printing which simplify the production of occlusal splints (Revilla-León and Özcan, 2019; Waldecker et al., 2019).

4.2. *High resolution single shot imaging*

The number of phase encoding steps in the used single-shot EPI sequence was minimized by a combination of reduced FOV acquisition with parallel imaging to reduce spatial distortions and signal blurring (Heidemann et al., 2012). Though, the need for additional saturation pulses in the zoomed protocols limited spatial coverage and resulted in low temporal efficiency due to SAR limitations. Therefore approaches like selective excitation with parallel transmit for 3D imaging (Poser et al., 2017) may be a better choice for reduced field of view acuisitions at ultra-high field in the future. With a sufficient number of slices, multi-band excitations can be incorporated as well to improve the efficiency and coverage of such approaches.

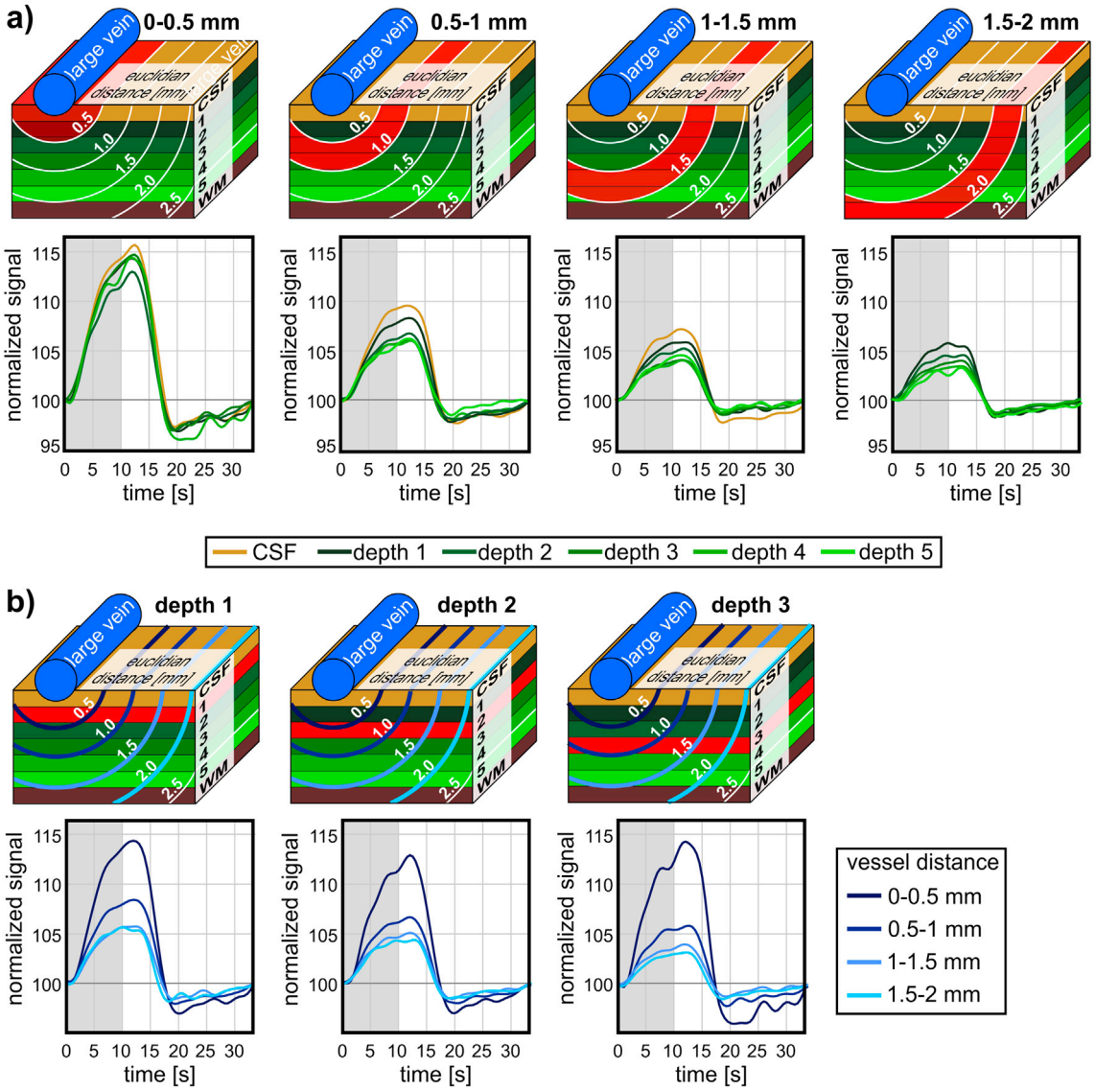

Fig. 8. Depth and large vein distance dependent BOLD responses from the same dataset shown as in Fig. 6b**, protocol C.** (a) Only a small gradient in signal amplitude across cortical depths is visible for iso-vessel distant voxels. Beside a slightly shorter response duration at larger vessel distances a reduction in post-stimulus undershoot can be observed. After reordering the plots to assess the vessel distance dependency within each depth, an even stronger increase in response amplitude near segmented vessels becomes visible (b).

4.3. Effects of local distortions on depth identification in EPI data

We found that local field perturbations near veins can vary rapidly and result in local displacements of up to several millimeters. This non-monotonic static field variations can lead to overlays of signal originating from different voxel positions during image acquisition already. Therefore, it cannot be corrected for using any post-processing technique. Potentially, this effect may lead to false positive activations several millimeters away from the actual side of signal change. However, these displacements can probably not sufficiently be captured using shiftmaps acquired at lower spatial resolution. Although the field perturbations can be captured at high resolution with conventional multi-echo GE data, this approach often suffers from phase wraps (Windischberger et al., 2004), open fringeline artifacts, and low SNR. For the latter reason, several averages are required in order to obtain a B_0-map with sufficient quality (e.g. to match the resolution of our PSF reference scan four averages are needed, data not shown), which would result in a longer acquisition time than needed for the PSF scan. In contrast, the PSF mapping scan allowed distortion mapping with high SNR efficiency at the same resolution as the EPI measurements. Another drawback of mapping distortions with the B_0-map approach, in the distortion free space, is the challenging ill-posed registration to the distorted EPI data (Zeng and Constable, 2002). This may explain results of several studies which showed that it is still difficult to reliably correct for severe local distortions using the voxel displacements acquired in the distortion free space (e.g. Fig. 6av and 6bv in Chung et al., 2011, Fig. 6 in Robinson and Jovicich, 2011, Figures 13 and 16 in In, 2012). In order to ensure alignment between the functional data and the distortion map scan, we employed prospective motion correction between the scans and corrected for motion during both scans. However, in cases where no PMC is available, the distorted reference data obtained from the reference scan, may be used for improved registration of the reference scan to the functional data due to identical geometric distortions like the functional data. Moreover, the distortion-free reference (calculated from the PSF scan) can be used for co-registration of the functional images to the anatomy.

In this study, we estimated more blurring of the BOLD signal after distortion correction using the PSF kernel compared to the PSF shiftmap and B_0 map based approach (Fig. 5). This can be explained by the fact

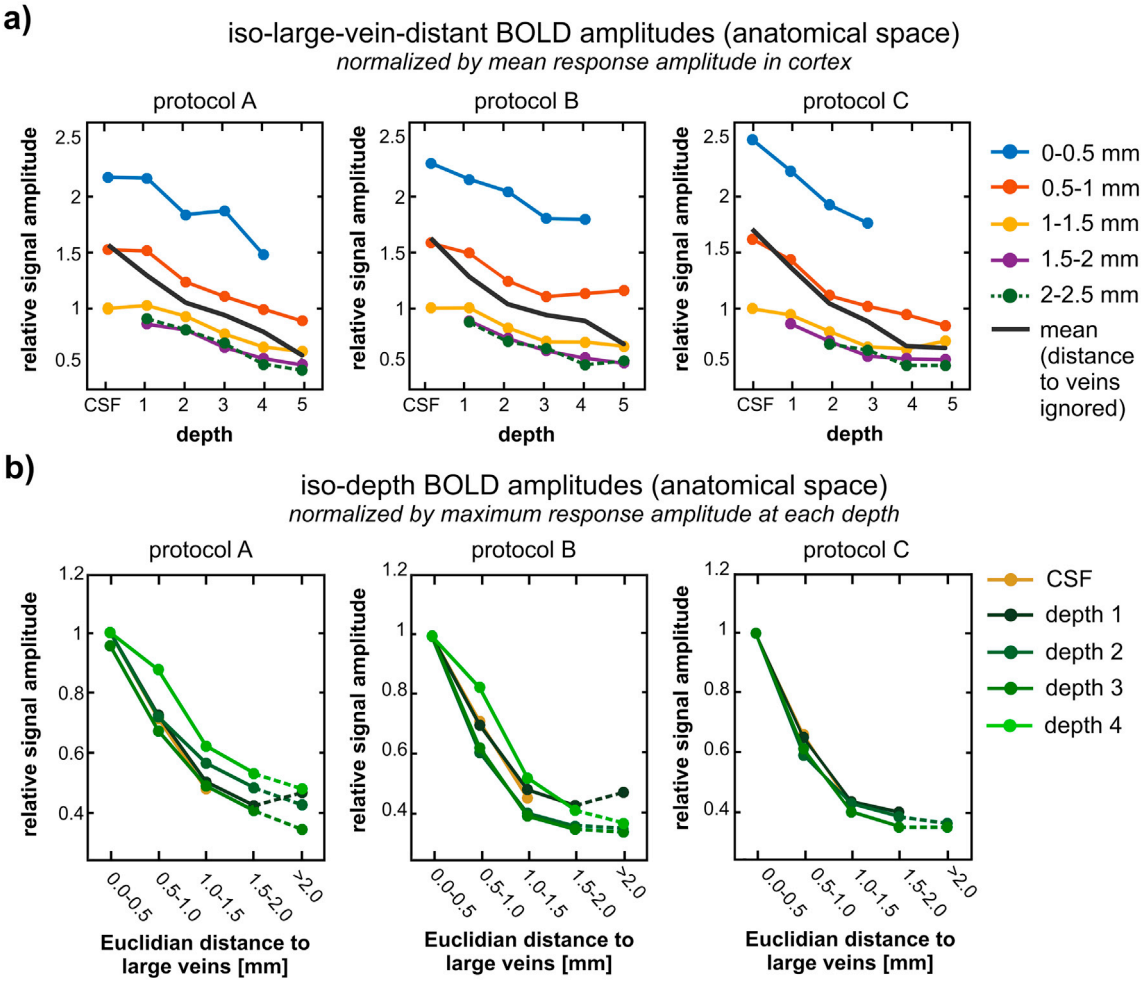

Fig. 9. Iso-vessel-distant and iso-depth relative BOLD amplitudes. The increase of the BOLD response amplitudes to the cortical surface are more pronounced near large veins than in areas having a large vessel distance (a). The gray line depicts the mean across subjects of the normalized signal amplitudes for different depths (see Fig. 7a). In (b), BOLD amplitudes for different vessel distances and cortical depth (averaged across subjects) are plotted. The dashed lines indicate values were data of less than three subjects was available because of an insufficient number of voxels within the ROIs.

Table 2
BOLD amplitude increase towards surface per depth.

large vein distance	Protocol A	Protocol B	Protocol C
0–0.5 mm	16.7%	13.6%	25.5%
0.5–1 mm	13.4%	10.9%	15.5%
1–1.5 mm	6.4%	7.9%	4.8%
1.5–2 mm	6.7%	8.6%	5.4%

that the magnitude rather than the complex PSF (Chaimow and Shmuel, 2016; Huber et al., 2015b) was used as an interpolation kernel (In and Speck, 2012). Therefore, the otherwise negative side lobes of the complex PSF were positive in case of the magnitude correction which lead to a wider FWHM. On the other hand, it can be expected that utilizing the phase in the PSF kernel makes the correction more sensitive to the image SNR and therefore spatial resolution as well as physiological noise fluctuations. Further investigation regarding this issue is therefore desirable. Nevertheless, we were able to minimize the interpolation blurring of the distortion correction by using the PSF shiftmap with comparable fidelity as the B_0 map based approach while the aforementioned issues were avoided. Although the effect of the stronger blurring was visible in the activation maps as well, the accuracy of the blurring estimation, as it was performed here, may be limited. This is due to the fact, that different interpolation methods were used for the distortion correction (cubic interpolation in case of the B_0- and PSF based shiftmap versus magnitude kernel weights in case of the PSF-Kernel correction).

An alternative way to perform distortion correction of functional data, would be to use distortion-matched T_1-weighted images for cortical segmentation to circumvent the reduction of spatial accuracy caused by dewarping the functional data to the anatomical space (Renvall et al., 2016). Recently, this distortion-matched method was found to be more accurate than warping anatomical data to the functional data using voxel shifts derived from a measurement with reversed phase-encoding (Kashyap et al., 2018). This showed that even if this 'reverse' approach is chosen to convert cortical depths calculated in the anatomical space to functional space, accurate distortion mapping and alignment of the voxel-shifts to the anatomy is essential.

4.4. Influence of large veins on cortical depth BOLD profiles

The majority of the vessels included in the analysis were likely large pial and cortical veins (Fig. 6). A cortical depth dependent effect of the GE-BOLD response can, however, be also expected from ascending veins which drain blood from varying cortical depths (Duvernoy et al., 1981; Markuerkiaga et al., 2016). Unfortunately, such ascending veins are very difficult to detect in V1 with MRI even at 400 μm isotropic resolution, most likely due to a smaller vessel diameter in areas with low cortical thickness (Fig. 6b). Thus, other cortical areas, like the primary motor cortex, may be more suitable to derive vascular masks for studying the influence of ascending veins on depth profiles in detail (Budde et al., 2014).

As expected, we observed an increase of the BOLD signal amplitude towards the cortical surface for all protocols used in this study (Fig. 7a). This amplitude variation is in agreement with the typical observations in laminar GE-BOLD measurements using comparable stimuli (Koopmans et al., 2010). The slope of this depth dependency varied slightly from subject to subject. Subjects with a large or small response amplitude in one protocol showed the same behavior for the others as well. These differences may have been caused in part by the variability of vessel orientations relative to the main magnetic field (De Martino et al., 2013; Goense et al., 2012). A comparison of the temporal characteristics of the response time courses yielded a stronger post-stimulus undershoot (PSU) at the cortical surface than in deep gray matter (Fig. 7b). Similar observations were made in studies performed at 7 T with lower spatial resolution (Siero et al., 2015). If the data was in addition sorted by the distance to large veins a stronger PSU near distance became visible and the cortical depth dependency of the PSU disappeared (Fig. 8).

Furthermore, in accordance with previous studies, a slight increase of response duration for more superficial depths was visible in the BOLD time courses (Fig. 7b) if the venous distance is not taken into account (Siero et al., 2013). On the other hand, it can be expected that the increase in response duration is independent of the distance to large veins if this effect is mainly driven by blood draining effects due to which superficial laminae contain deoxygenated blood originating from the same depth and deeper laminae (Heinzle et al., 2016). Here, we observed almost no difference in response duration if the voxels were sorted according to the large vein distance (Fig. 8a). Thus, the influence of draining vein effects on the response duration was probably small. Usually, no intravascular venous signal can be observed with GE-EPI at ultra-high field due to the short T_2 of venous blood. However, susceptibility changes near large veins can still be a major component in the functional signal sampled from the cortex (e.g. Hoogenrad et al., 2001; Kay et al., 2018; Koopmans et al., 2010). We observed that the BOLD amplitude decreases for increasing distance to large veins even in large depths (Figs. 8 and 9a). A detailed investigation showed an up to 2.2 times higher signal amplitude near large veins (distance <0.5 mm) than in similar depths at larger vessel distances. This influence from large veins declined rapidly with increasing distance and leveled out at a vessel distance of 1–1.5 mm (Fig. 9b). Still, this means that approximately 33% of all cortical voxels are expected to show contributions from large veins in case of GE-BOLD at 9.4 T for the chosen sequence parameters. On the other hand, the slight slope in signal amplitude towards the cortical surface even distant from large veins (Fig. 8a and Table 2) can be explained by the mentioned draining vein effects which indicates that this effect plays only a minor role in GE-BOLD laminar studies.

A number of techniques were proposed to reduce venous contributions from large cortical and pial veins or ascending veins in cortical signal profiles. To remove effects from large veins, one group suggested to sort depth profiles according their linearity in signal increase towards cortical surface (Fracasso et al., 2017). If only profiles with a weak linear correlation are taken into account (in (Fracasso et al., 2017) lowest 40% quantile of the Pearson correlation), areas affected by spatially inaccurate influences of pial veins can be successfully excluded. Although more detailed studies are required, it can be expected that this approach for the removal of macrovascular biases is quite robust, since mainly regions within approximately 1 mm from large veins showed a cortical depth dependency in this study as well (Fig. 9, Table 2). A correction for the influence of ascending veins can be performed by normalizing the depth profiles of an 'advanced' stimulus with the depth profiles measured during a 'calibration' stage consisting of a simple stimulus (Kashyap et al., 2018) or hypercapnia experiment (Guidi et al., 2016). This method is based on the assumption that the depth dependence of response amplitudes is mainly caused by intracortical variations in cerebral blood volume (CBV) and variations in venous blood oxygenation in ascending veins (Uludağ and Blinder, 2018). It may therefore be more effective than the subtraction of laminar signal gradients (Polimeni et al., 2010). However, based on our observations about the influence of large veins, we think that additional validation of methods correcting for ascending vein effects against the influences of large veins may be necessary.

It is well known that the capillary and non-capillary vessel density in layer IV is higher than in any other layer of V1, leading to a particularly high vascular volume fraction in these areas (Duvernoy et al., 1981; Weber et al., 2008). In addition, in case of high contrast visual stimulation, the maximum neuronal activity in V1 can be expected in cortical layer IV, since it receives the input from lateral geniculate nucleus (Hubel and Wiesel, 1972). Thus, if there is a tight link between neuronal activity and functional changes, one would expect the largest fMRI signal change in the corresponding depth as well. Although another study measured the maximum signal changes centered between the WM/GM and GM/CSF boundary after excluding venous signal from their analysis (Koopmans et al., 2010), no such observation was made in this study for any of the protocols even for voxels far distant from large veins. However, due to the complex neurovascular coupling mechanisms and the much faster spreading of neuronal signals within the cortex compared to the BOLD response it is still debated whether the maximum BOLD response can be actually expected in layer IV solely due to a higher CBV (e.g. see discussion in (Koopmans et al., 2010)).

It is also important to note that some post-processing steps can affect the spatial extend of signal contributions, too. This makes it even more difficult to compare results from different studies. For example, any venous effects will be spread further if smoothing is used, and "laminar smoothing" restricted to specific depths has been advocated in laminar fMRI studies (Blazejewska et al., 2019; Huber et al., 2017). On the other hand, gaining knowledge about the spatiotemporal relationship of the BOLD signal and the cortical venous network may also improve the verification of simulation models and can help to get a better understanding about the specificity of other contrasts, like spin-echo or bSSFP BOLD, to different vessel sizes and the resulting spatial accuracy (Báez-Yánez et al., 2017). Taking large veins as confounding factors into account potentially also changes the way how resting-state MRI data is interpreted. For instance, a recent report showed that low frequency oscillations in resting-state fMRI are dominantly originating from the macro-vasculature (Guidi et al., 2017).

4.5. Possible confounds of this study

In this study, large veins were segmented with a Hessian based filter applied on the SWI. Although visual inspection showed that the filter was successful in detecting large veins in the visual cortex ROI of all subjects (Supplementary Fig. A.8), the performance of this filter dependents strongly on image noise level, spatial signal homogeneity and the size of the vessels relative to the scale of the Hessian filter kernel. Filter functions which utilize multi-echo data to improve robustness may therefore be preferred for studies with larger spatial coverage and regions with strong signal variations (Monti et al., 2017). Another option to use a Gaussian Mixture model to filter for 'dark' voxels in the mean of the EPI time-series (Kay et al., 2018). Moreover, it is important to keep in mind, that veins appear larger than they actually are due to their extended susceptibility effects in images with strong T_2*-weighting. On one hand, this makes the vessel mask even more conservative and allows to detect vessels with a small diameter, but on the other hand, it complicates the differentiation between actual tissue and veins. Calculating venous diameters from quantitative susceptibility data (Bazin et al., 2016; Huck et al., 2019) may thus help to further improve the precision of quantification of venous influences on fMRI. Incorporating a vein mask is likely to be beneficial for automatic cortical segmentation as well, since longitudinal relaxation times of venous blood and highly myelinated gray matter (like in V1) are almost similar. This can be also seen in Fig. 4 b and c, where the sagittal sinus can barely be separated from cortical tissue.

It may be also criticized that we applied an activation mask which was then extended along the cortical normal axis. Other laminar studies avoided the use of any thresholded activation map and incorporated anatomical landmarks (Huber et al., 2015) or projected brain atlases

instead (Kay et al., 2018). For our approach, a slightly larger fraction of voxels located proximal to large veins than in the volume covered by the anatomical gradient-echo measurement was observed (Fig. 6d). Since, at the same time, the distributions for the individual cortical depths were almost identical, we assume that this difference was caused by the smaller cortical depth in the visual cortex.

A more detailed investigation of the venous influences on laminar BOLD also requires a comparison to spin-echo measurements in which macrovascular influences are expected to be minimized. However, SE-EPI is still challenging at high field strengths due to high SAR, B_1^+-inhomogeneities and reduced functional contrast (Budde et al., 2014). In addition, SE-EPIs can still contain residual T_2*-weighting due to the long echo train. Therefore, GRASE was suggested as an alternative (Kemper et al., 2015). The reduced signal contributions from large veins and resulting increased spatial specificity were recently also demonstrated in an auditory study comparing GE-EPI and GRASE (Moerel et al., 2018).

5. Conclusions

We showed that the cortical depth profiles for the different spatial resolutions (800 μm isotropic versus 650 μm isotropic) and the echo train lengths (35 ms versus 41 ms) are comparable. Since imaging at 800 μm isotropic resolution with high parallel imaging factors provides the higher tSNR and allows for better temporal resolution than imaging with outer volume suppression, it should be the preferred approach in future laminar fMRI studies with 2D GE-EPI. This is especially the case if the image analysis can be performed in native EPI space where the larger distortions are not as problematic.

Beside an automatic registration of individual runs and reference scans the prospective motion correction reduced the variation of residual motion across subjects. However, since the retrospectively image based estimated motion was larger than the nominal accuracy of the tracking system and above the potential error of the retrospective correction, we think that using only PMC for the correction of image displacements may not always be sufficient in high resolution experiments. Hence, in some cases an additional retrospective correction may still be required to compensate for insufficiently corrected non-subject motion related image displacements.

We also investigated whether the higher fidelity of the PSF-mapping method compared to a correction based on low resolution B_0 maps is translated to improved spatial accuracy. Although the magnitude PSF correction technique used in this study did not allow correcting for T_2*-blurring and resulted in resolution losses in case of image dewarping based on the magnitude kernel, we believe that correction based on PSF mapping is preferable over correction based on a low resolution B_0 map. One main benefit is that, in addition to the voxel shifts, GE-like and EPI-like high SNR images can be derived from the reference scan. Due to the similar T_2*-weighting as the functional data, the additional images are perfectly suited for an accurate co-registration of distortion mapping and functional images when no PMC is available. The voxel shiftmaps derived from the PSF measurements furthermore showed that the distortions occurring proximal to large veins can lead to an overlay of signals originating from different spatial positions. Although this effect cannot be corrected during postprocessing, the additional information provided by a high-resolution shiftmap may allow to exclude affected voxels to improve spatial accuracy further.

This study also showed that the GE-EPI BOLD amplitude as well as the PSU is strongly dependent on the proximity to large veins. Yet, even within areas distant from large veins a depth dependency of the functional signal is still present. Thus, the different influences of large veins and ascending cortical veins on the spatial accuracy of GE-BOLD are difficult to separate. Nevertheless, the methods used here can help to investigate the robustness of correction methods for vascular effects in the future and may allow for detailed investigation of the underlying signal contributions in other fMRI contrasts as well.

Acknowledgements

The authors thank the reviewers for their helpful comments, Maxim Zaitsev, Department of Radiology, University of Freiburg, Germany, for his support during setting up the prospective motion correction system. Eva-Maria Engel and Ekkehard Kroewerath, Department for Prosthodontics, University of Tuebingen, for their help in optimizing the design and building the occlusal splints. This work was funded in part by the DFG, a Reinhart Koselleck Project, DFG SCHE 658/12, DFG SCHE 658/15, and by the Max Planck Society. J.R.P. was supported in part by the NIH NIBIB (grant R01-EB019437) and by the BRAIN Initiative (NIH NIMH grant R01-MH111419).

Parts of this work were presented at the ISMRM 2015 and ESMRMB 2017.

Appendix A. Supplementary data

Supplementary data to this article can be found online at https://doi.org/10.1016/j.neuroimage.2019.116434.

References

Aghaeifar, A., Bause, J., Mirkes, C., Steffen, T., Avdievitch, N., Henning, A., Scheffler, K., 2018. Dynamic B 0 shimming of the human brain at 9.4 T with a 16-channel multi-coil shim setup. Magn. Reson. Med. 80, 1714–1725. https://doi.org/10.1002/mrm.27110.

Aghaeifar, A., Eschelbach, M., Bause, J., Thielscher, A., Scheffler, K., 2017. AMoCo, a software package for prospective motion correction. Proc. Intl. Soc. Mag. Reson. Med. 25, 305.

Andersson, J.L.R., Skare, S., Ashburner, J., 2003. How to correct susceptibility distortions in spin-echo echo-planar images: application to diffusion tensor imaging. Neuroimage 20, 870–888. https://doi.org/10.1016/S1053-8119(03)00336-7.

Báez-Yánez, M.G., Ehses, P., Mirkes, C., Tsai, P.S., Kleinfeld, D., Scheffler, K., 2017. The impact of vessel size, orientation and intravascular contribution on the neurovascular fingerprint of BOLD bSSFP fMRI. Neuroimage 163, 13–23. https://doi.org/10.1016/j.neuroimage.2017.09.015.

Bazin, P.-L., Weiss, M., Dinse, J., Schäfer, A., Trampel, R., Turner, R., 2014. A computational framework for ultra-high resolution cortical segmentation at 7Tesla. Neuroimage 93 Pt 2, 201–209. https://doi.org/10.1016/j.neuroimage.2013.03.077.

Bazin, P.L., Plessis, V., Fan, A.P., Villringer, A., Gauthier, C.J., 2016. Vessel segmentation from quantitative susceptibility maps for local oxygenation venography. Proc. - Int. Symp. Biomed. Imaging 1135–1138. https://doi.org/10.1109/ISBI.2016.7493466.

Berman, A.J., Witzel, T., Grissom, W.A., Park, D., Setsompop, K., Polimeni, J.R., 2019. High-resolution segmented-accelerated EPI using Variable Flip Angle FLEET with tailored slice profiles. Proc. Intl. Soc. Mag. Reson. Med. 27, 1169.

Blazejewska, A.I., Fischl, B., Wald, L.L., Polimeni, J.R., 2019. Intracortical smoothing of small-voxel fMRI data can provide increased detection power without spatial resolution losses compared to conventional large-voxel fMRI data. Neuroimage 189, 601–614. https://doi.org/10.1016/j.neuroimage.2019.01.054.

Breuer, F., Blaimer, M., Heidemann, R.M., Mueller, M.F., Griswold, M., Jakob, P.M., 2005. Controlled aliasing in parallel imaging results in higher acceleration (CAIPIRINHA) for multi-slice imaging. Magn. Reson. Med. 53, 684–691. https://doi.org/10.1002/mrm.20401.

Budde, J., Shajan, G., Zaitsev, M., Scheffler, K., Pohmann, R., 2014. Functional MRI in human subjects with gradient-echo and spin-echo EPI at 9.4 T. Magn. Reson. Med. 71, 209–218. https://doi.org/10.1002/mrm.24656.

Chaimow, D., Shmuel, A., 2016. A more accurate account of the effect of k-space sampling and signal decay on the effective spatial resolution in functional MRI. bioRxivio 1–35. https://doi.org/10.1101/097154.

Chung, J.Y., In, M.H., Oh, S.H., Zaitsev, M., Speck, O., Cho, Z.H., 2011. An improved PSF mapping method for EPI distortion correction in human brain at ultra high field (7T). Magn. Reson. Mater. Physics, Biol. Med. 24, 179–190. https://doi.org/10.1007/s10334-011-0251-1.

De Martino, F., Zimmermann, J., Muckli, L., Ugurbil, K., Yacoub, E., Goebel, R., 2013. Cortical depth dependent functional responses in humans at 7T: improved specificity with 3D GRASE. PLoS One 8, e60514. https://doi.org/10.1371/journal.pone.0060514.

Duvernoy, H.M., Delon, S., Vannson, J.L., 1981. Cortical blood vessels of the human brain. Brain Res. Bull. 7, 519–579. https://doi.org/10.1016/0361-9230(81)90007-1.

Dymerska, B., Poser, B.A., Barth, M., Trattnig, S., Robinson, S.D., 2018. A method for the dynamic correction of B0-related distortions in single-echo EPI at 7 T. Neuroimage 168, 321–331. https://doi.org/10.1016/j.neuroimage.2016.07.009.

Finsterbusch, J., 2013. Functional neuroimaging of inner fields-of-view with 2D-selective RF excitations. Magn. Reson. Imaging 31, 1228–1235. https://doi.org/10.1016/j.mri.2013.03.005.

Fracasso, A., Luijten, P.R., Dumoulin, S.O., Petridou, N., 2017. Laminar imaging of positive and negative BOLD in human visual cortex at 7T. Neuroimage 1–12. https://doi.org/10.1016/j.neuroimage.2017.02.038.

Frangi, A.F., Niessen, W.J., Vincken, K.L., Viergever, M.A., 1998. Multiscale vessel enhancement filtering. Med. Image Comput. Comput. Interv. 130–137. https://doi.org/10.1007/BFb0056195.

Friston, K.J., Williams, S., Howard, R., Frackowiak, R.S., Turner, R., 1996. Movement-related effects in fMRI time-series. Magn. Reson. Med. 35, 346–355. https://doi.org/10.1002/mrm.1910350312.

Goa, P.E., Koopmans, P.J., Poser, B.A., Barth, M., Norris, D.G., 2014. Bold fMRI signal characteristics of S1- and S2-SSFP at 7 Tesla. Front. Neurosci. 8, 1–6. https://doi.org/10.3389/fnins.2014.00049.

Goense, J., Merkle, H., Logothetis, N.K., 2012. High-resolution fMRI reveals laminar differences in neurovascular coupling between positive and negative BOLD responses. Neuron 76, 629–639. https://doi.org/10.1016/j.neuron.2012.09.019.

Gorgolewski, K., Burns, C.D., Madison, C., Clark, D., Halchenko, Y.O., Waskom, M.L., Ghosh, S.S., 2011. Nipype: a flexible, lightweight and extensible neuroimaging data processing framework in Python. Front. Neuroinf. 5. https://doi.org/10.3389/fninf.2011.00013.

Griswold, M. a, Jakob, P.M., Heidemann, R.M., Nittka, M., Jellus, V., Wang, J., Kiefer, B., Haase, A., 2002. Generalized autocalibrating partially parallel acquisitions (GRAPPA). Magn. Reson. Med. 47, 1202–1210. https://doi.org/10.1002/mrm.10171.

Guidi, M., Huber, L., Lampe, L., Gauthier, C.J., Möller, H.E., 2016. Lamina-dependent calibrated BOLD response in human primary motor cortex. Neuroimage 141, 250–261. https://doi.org/10.1016/j.neuroimage.2016.06.030.

Guidi, M., Markuerkiaga, I., Bains, L., Huber, L., Möller, H.E., Norris, D.G., 2017. Frequency signature of cortical laminar fMRI. Proc. Intl. Soc. Mag. Reson. Med. 25, 158.

Haacke, E., Lindskogj, E., Lin, W., 1991. A fast, iterative, partial-fourier technique capable of local phase recovery. J. Magn. Reson. 92, 126–145. https://doi.org/10.1016/0022-2364(91)90253-P.

Haast, R.A.M., Ivanov, D., Uludağ, K., 2018. The impact of B1+ correction on MP2RAGE cortical T1and apparent cortical thickness at 7T. Hum. Brain Mapp. 39, 2412–2425. https://doi.org/10.1002/hbm.24011.

Hagberg, G., Bause, J., Ethofer, T., Ehses, P., Dresler, T., Herbert, C., Pohmann, R., Shajan, G., Fallgatter, A., Pavlova, M., Scheffler, K., 2016. Whole brain MP2RAGE-based mapping of the longitudinal relaxation time at 9.4T. Neuroimage 144, 203–216. https://doi.org/10.1016/j.neuroimage.2016.09.047.

Heidemann, R.M., Ivanov, D., Trampel, R., Fasano, F., Meyer, H., Pfeuffer, J., Turner, R., 2012. Isotropic submillimeter fMRI in the human brain at 7 T: combining reduced field-of-view imaging and partially parallel acquisitions. Magn. Reson. Med. 68, 1506–1516. https://doi.org/10.1002/mrm.24156.

Heinzle, J., Koopmans, P.J., den Ouden, H.E.M., Raman, S., Stephan, K.E., 2016. A hemodynamic model for layered BOLD signals. Neuroimage 125, 556–570. https://doi.org/10.1016/j.neuroimage.2015.10.025.

Hoogenrad, F.G.C., Pouwels, P.J.W., Hofman, M.B.M., Reichenbach, J.R., Sprenger, M., Haacke, E.M., 2001. Quantitative differentiation between BOLD models in fMRI. Magn. Reson. Med 45, 233–246. https://doi.org/10.1002/1522-2594(200102)45:2<233::AID-MRM1032>3.0.CO;2-W.

Hubel, D.H., Wiesel, T.N., 1972. Laminar and columnar distribution of geniculo-cortical fibers in the macaque monkey. J. Comp. Neurol. 146, 421–450.

Huber, L., Goense, J., Kennerley, A.J., Trampel, R., Guidi, M., Reimer, E., Ivanov, D., Neef, N., Gauthier, C.J., Turner, R., Möller, H.E., 2015a. Cortical lamina-dependent blood volume changes in human brain at 7T. Neuroimage 107, 23–33. https://doi.org/10.1016/j.neuroimage.2014.11.046.

Huber, L., Guidi, M., Goense, J., Mildner, T., Trampel, R., Schulz, J., Eichner, C., Turner, R., Möller, H.E., 2015b. The magnitude point spread function is an inadequate measure of T2*-blurring in EPI. 23nd. Annu. Meet. ISMRM 23, 2056.

Huber, L., Handwerker, D. a, Jangraw, D.C., Chen, G., Hall, A., Stüber, C., Gonzalez-Castillo, J., Ivanov, D., Marrett, S., Guidi, M., Goense, J.B.M., Poser, B.A., Bandettini, P.A., 2017. High-resolution CBV-fMRI allows mapping of laminar activity and connectivity of cortical input and output in human M1. Neuron 1–11. https://doi.org/10.1016/j.neuron.2017.11.005.

Huck, J., Wanner, Y., Fan, A.P., Schmidt, A.-T., Grahl, S., Schneider, U., Villringer, A., Steele, C.J., Tardif, C.L., Bazin, P.-L., Gaulthier, C.J., 2019. High resolution atlas of the venous brain vasculature from 7 T quantitative susceptibility maps. Brain Struct. Funct. 224 (7), 2467–2485. https://doi.org/10.1007/s00429-019-01919-4.

Hurley, A.C., Al-Radaideh, A., Bai, L., Aickelin, U., Coxon, R., Glover, P., Gowland, P.A., 2010. Tailored RF pulse for magnetization inversion at ultrahigh field. Magn. Reson. Med. 63, 51–58. https://doi.org/10.1002/mrm.22167.

Hwang, T.L., van Zijl, P.C., Garwood, M., 1999. Asymmetric adiabatic pulses for NH selection. J. Magn. Reson. 138, 173–177. https://doi.org/10.1006/jmre.1999.1713.

In, M.-H., 2012. Geometric distortion correction in EPI at ultra high field. Universitaet Magdeburg (Dissertation).

In, M.H., Speck, O., 2012. Highly accelerated PSF-mapping for EPI distortion correction with improved fidelity. Magn. Reson. Mater. Physics, Biol. Med. 25, 183–192. https://doi.org/10.1007/s10334-011-0275-6.

Jezzard, P., Balaban, R.S., 1995. Correction for geometric distortion in echo planar images from B0 field variations. Magn. Reson. Med. 34, 65–73. https://doi.org/10.1002/mrm.1910340111.

Jezzard, P., Clare, S., 1999. Sources of distortion in functional MRI data. Hum. Brain Mapp. 8, 80–85. https://doi.org/10.1002/(SICI)1097-0193(1999)8:2/3<80::AID-HBM2>3.0.CO;2-C.

Kashyap, S., Ivanov, D., Havlicek, M., Poser, B.A., Uludağ, K., 2018. Impact of acquisition and analysis strategies on cortical depth-dependent fMRI. Neuroimage 168, 332–344. https://doi.org/10.1016/j.neuroimage.2017.05.022.

Kay, K., Jamison, K., Vizioli, L., Zhang, R., Margalit, E., Ugurbil, K., 2018. A critical assessment of data quality and venous effects in ultra-high-resolution fMRI 1–45. https://doi.org/10.1101/337667.

Kemper, V.G., De Martino, F., Emmerling, T.C., Yacoub, E., Goebel, R., 2018. High resolution data analysis strategies for mesoscale human functional MRI at 7 and 9.4 T. Neuroimage 164, 48–58. https://doi.org/10.1016/j.neuroimage.2017.03.058.

Kemper, V.G., De Martino, F., Vu, A.T., Poser, B., Feinberg, D., Goebel, R., Yacoub, E., 2015. Sub-millimeter T2 weighted fMRI at 7 T: comparison of 3D-GRASE and 2D SE-EPI. Front. Neurosci. 9, 1–14. https://doi.org/10.3389/fnins.2015.00163.

Koopmans, P.J., Barth, M., Norris, D.G., 2010. Layer-specific BOLD activation in human V1. Hum. Brain Mapp. 31, 1297–1304. https://doi.org/10.1002/hbm.20936.

Koopmans, P.J., Barth, M., Orzada, S., Norris, D.G., 2011. Multi-echo fMRI of the cortical laminae in humans at 7T. Neuroimage 56, 1276–1285. https://doi.org/10.1016/j.neuroimage.2011.02.042.

Kroon, D.-J., 2009. Hessian based frangi vesselness filter [WWW Document]. URL. https://www.mathworks.com/matlabcentral/fileexchange/24409-hessian-based-frangi-vesselness-filter (accessed 7.20.19).

Lawrence, S.J.D., Formisano, E., Muckli, L., de Lange, F.P., 2017. Laminar fMRI: applications for cognitive neuroscience. Neuroimage 1–7. https://doi.org/10.1016/j.neuroimage.2017.07.004.

Maclaren, J., Armstrong, B.S.R., Barrows, R.T., Danishad, K., Ernst, T., Foster, C.L., Gumus, K., Herbst, M., Kadashevich, I.Y., Kusik, T.P., Li, Q., Lovell-Smith, C., Prieto, T., Schulze, P., Speck, O., Stucht, D., Zaitsev, M., 2012. Measurement and correction of microscopic head motion during magnetic resonance imaging of the brain. PLoS One 7, 3–11. https://doi.org/10.1371/journal.pone.0048088.

Maclaren, J., Herbst, M., Speck, O., Zaitsev, M., 2013. Prospective motion correction in brain imaging: a review. Magn. Reson. Med. 69, 621–636. https://doi.org/10.1002/mrm.24314.

Markuerkiaga, I., Barth, M., Norris, D.G., 2016. A cortical vascular model for examining the specificity of the laminar BOLD signal. Neuroimage 132, 491–498. https://doi.org/10.1016/j.neuroimage.2016.02.073.

Marques, J.P., Kober, T., Krueger, G., van der Zwaag, W., Van de Moortele, P.F., Gruetter, R., 2010. MP2RAGE, a self bias-field corrected sequence for improved segmentation and T1-mapping at high field. Neuroimage 49, 1271–1281. https://doi.org/10.1016/j.neuroimage.2009.10.002.

Martinez Santiesteban, F., Swanson, S., Noll, D., Anderson, D., 2006. Object orientation independence of Susceptibility Weighted Imaging by using a Sigmoid-type phase window. Proc Intl Soc Mag Reson Med 24, 2399.

Moerel, M., De Martino, F., Kemper, V.G., Schmitter, S., Vu, A.T., Uğurbil, K., Formisano, E., Yacoub, E., 2018. Sensitivity and specificity considerations for fMRI encoding, decoding, and mapping of auditory cortex at ultra-high field. Neuroimage 164, 18–31. https://doi.org/10.1016/j.neuroimage.2017.03.063.

Monti, S., Cocozza, S., Borrelli, P., Straub, S., Ladd, M.E., Salvatore, M., Tedeschi, E., Palma, G., 2017. MAVEN: an algorithm for multi-parametric automated segmentation of brain veins from gradient echo acquisitions. IEEE Trans. Med. Imaging 36, 1054–1065. https://doi.org/10.1109/TMI.2016.2645286.

Muraskin, J., Ooi, M.B., Goldman, R.I., Krueger, S., Thomas, W.J., Sajda, P., Brown, T.R., 2013. Prospective active marker motion correction improves statistical power in BOLD fMRI. Neuroimage 68, 154–161. https://doi.org/10.1016/j.neuroimage.2012.11.052.

Oakes, T.R., Johnstone, T., Ores Walsh, K.S., Greischar, L.L., Alexander, aL, Fox, aS, Davidson, R.J., 2005. Comparison of fMRI motion correction software tools. Neuroimage 28, 529–543. https://doi.org/10.1016/j.neuroimage.2005.05.058.

Ooi, M.B., Muraskin, J., Zou, X., Thomas, W.J., Krueger, S., Aksoy, M., Bammer, R., Brown, T.R., 2013. Combined prospective and retrospective correction to reduce motion-induced image misalignment and geometric distortions in EPI. Magn. Reson. Med. 69, 803–811. https://doi.org/10.1002/mrm.24285.

Petridou, N., Siero, J.C.W., 2017. Laminar fMRI: what can the time domain tell us? Neuroimage 1–11. https://doi.org/10.1016/j.neuroimage.2017.07.040.

Pfeuffer, J., van de Moortele, P.-F., Ugurbil, K., Hu, X., Glover, G.H., 2002. Correction of physiologically induced global off- resonance effects in dynamic echo-planar and spiral. Funct. Imaging 353, 344–353. https://doi.org/10.1002/mrm.10065.

Pfeuffer, J., van de Moortele, P.-F., Yacoub, E., Shmuel, A., Adriany, G., Andersen, P., Merkle, H., Garwood, M., Ugurbil, K., Hu, X., 2002. Zoomed Functional Imaging in the Human Brain at 7 Tesla with Simultaneous High Spatial and High Temporal Resolution. NeuroImage 17, 272–286. https://doi.org/10.1006/nimg.2002.1103.

Pohmann, R., Speck, O., Scheffler, K., 2016. Signal-to-Noise Ratio and MR tissue parameters in human brain imaging at 3, 7, and 9.4 Tesla using current receive coil arrays. Magn. Reson. Med. 75 (2), 801–809. https://doi.org/10.1002/mrm.25677.

Polimeni, J.R., Bhat, H., Witzel, T., Benner, T., Feiweier, T., Inati, S.J., Renvall, V., Heberlein, K., Wald, L.L., 2016. Reducing sensitivity losses due to respiration and motion in accelerated echo planar imaging by reordering the autocalibration data acquisition. Magn. Reson. Med. 75, 665–679. https://doi.org/10.1002/mrm.25628.

Polimeni, J.R., Fischl, B., Greve, D.N., Wald, L.L., 2010. Laminar analysis of 7 T BOLD using an imposed spatial activation pattern in human V1. Neuroimage 52, 1334–1346. https://doi.org/10.1016/j.neuroimage.2010.05.005.

Polimeni, J.R., Renvall, V., Zaretskaya, N., Fischl, B., 2018. Analysis strategies for high-resolution UHF-fMRI data. Neuroimage 168, 296–320. https://doi.org/10.1016/j.neuroimage.2017.04.053.

Poser, B.A., Kaas, A.L., Wiggins, C.J., Uludag, K., Tse, D.H.Y., 2017. Dual region-selective spiral pTX excitation for digit mapping fMRI in motor cortex and cerebellum. Proc. Intl. Soc. Mag. Reson. Med. 25, 588.

Pruessmann, K.P., Weiger, M., Scheidegger, M.B., Boesiger, P., 1999. SENSE: sensitivity encoding for fast MRI. Magn. Reson. Med. 42, 952–962. https://doi.org/10.1002/(SICI)1522-2594(199911)42:5<952::AID-MRM16>3.0.CO;2-S.

Reber, P.J., Wong, E.C., Buxton, R.B., Frank, L.R., 1998. Correction of off resonance-related distortion in echo-planar imaging using EPI-based field maps. Magn. Reson. Med. 39, 328–330. https://doi.org/10.1002/mrm.1910390223.

Renvall, V., Witzel, T., Wald, L.L., Polimeni, J.R., 2016. Automatic cortical surface reconstruction of high-resolution T1 echo planar imaging data. Neuroimage 134, 338–354. https://doi.org/10.1016/j.neuroimage.2016.04.004.

Ress, D., Glover, G.H., Liu, J., Wandell, B., 2007. Laminar profiles of functional activity in the human brain. Neuroimage 34, 74–84. https://doi.org/10.1016/j.neuroimage.2006.08.020.

Revilla-León, M., Özcan, M., 2019. Additive manufacturing technologies used for processing polymers: current status and potential application in Prosthetic dentistry. J. Prosthodont. 28, 146–158. https://doi.org/10.1111/jopr.12801.

Robinson, S., Jovicich, J., 2011. B0 mapping with multi-channel RF coils at high field. Magn. Reson. Med. 66, 976–988. https://doi.org/10.1002/mrm.22879.

Robson, M.D., Gore, J.C., Constable, R.T., 1997. Measurement of the point spread function in MRI using constant time imaging. Magn. Reson. Med. 38, 733–740.

Scheffler, K., Heule, R., Báez-Yánez, M.G., Kardatzki, B., Lohmann, G., 2019. The BOLD sensitivity of rapid steady-state sequences. Magn. Reson. Med. 81, 2526–2535. https://doi.org/10.1002/mrm.27585.

Schulz, J., Siegert, T., Bazin, P.L., Maclaren, J., Herbst, M., Zaitsev, M., Turner, R., 2014. Prospective slice-by-slice motion correction reduces false positive activations in fMRI with task-correlated motion. Neuroimage 84, 124–132. https://doi.org/10.1016/j.neuroimage.2013.08.006.

Shajan, G., Kozlov, M., Hoffmann, J., Turner, R., Scheffler, K., Pohmann, R., 2013. A 16-channel dual-row transmit array in combination with a 31-element receive array for human brain imaging at 9.4 T. Magn. Reson. Med. 879, 870–879. https://doi.org/10.1002/mrm.24726.

Siero, J.C.W., Hendrikse, J., Hoogduin, H., Petridou, N., Luijten, P., Donahue, M.J., 2015. Cortical depth dependence of the BOLD initial dip and poststimulus undershoot in human visual cortex at 7 Tesla. Magn. Reson. Med. 73, 2283–2295. https://doi.org/10.1002/mrm.25349.

Siero, J.C.W., Petridou, N., Hoogduin, H., Luijten, P.R., Ramsey, N.F., 2011. Cortical depth-dependent temporal dynamics of the BOLD response in the human brain. J. Cereb. Blood Flow Metab. 31, 1999–2008. https://doi.org/10.1038/jcbfm.2011.57.

Siero, J.C.W., Ramsey, N.F., Hoogduin, H., Klomp, D.W.J., Luijten, P.R., Petridou, N., 2013. BOLD specificity and dynamics evaluated in humans at 7 T: comparing gradient-echo and spin-echo hemodynamic responses. PLoS One 8, 1–8. https://doi.org/10.1371/journal.pone.0054560.

Speck, O., Stadler, J., Zaitsev, M., 2008. High resolution single-shot EPI at 7T. Magn. Reson. Mater. Physics, Biol. Med. 21, 73–86. https://doi.org/10.1007/s10334-007-0087-x.

Stockmann, J.P., Witzel, T., Keil, B., Polimeni, J.R., Mareyam, A., LaPierre, C., Setsompop, K., Wald, L.L., 2015. A 32-channel combined RF and B 0 shim array for 3T brain imaging. Magn. Reson. Med. 75, 441–451. https://doi.org/10.1002/mrm.25587.

Thesen, S., Heid, O., Mueller, E., Schad, L.R., 2000. Prospective acquisition correction for head motion with image-based tracking for real-time fMRI. Magn. Reson. Med. 44, 457–465. https://doi.org/10.1002/1522-2594(200009)44:3<457::AID-MRM17>3.0.CO;2-R.

Todd, N., Josephs, O., Callaghan, M.F., Lutti, A., Weiskopf, N., 2015. Prospective motion correction of 3D echo-planar imaging data for functional MRI using optical tracking. Neuroimage 113, 1–12. https://doi.org/10.1016/j.neuroimage.2015.03.013.

Triantafyllou, C., Hoge, R.D., Krueger, G., Wiggins, C.J., Potthast, A., Wiggins, G.C., Wald, L.L., 2005. Comparison of physiological noise at 1.5 T, 3 T and 7 T and optimization of fMRI acquisition parameters. Neuroimage 26, 243–250. https://doi.org/10.1016/j.neuroimage.2005.01.007.

Turner, R., 2002. How much cortex can a vein drain? Downstream dilution of activation-related cerebral blood oxygenation changes. Neuroimage 16, 1062–1067. https://doi.org/10.1006/nimg.2002.1082.

Turner, R., Jezzard, P., Wen, H., Kwong, K.K., Le Bihan, D., Zeffiro, T., Balaban, R.S., 1993. Functional mapping of the human visual cortex at 4 and 1.5 tesla using deoxygenation contrast EPI. Magn. Reson. Med. 29, 277–279. https://doi.org/10.1002/mrm.1910290221.

Uludağ, K., Blinder, P., 2018. Linking brain vascular physiology to hemodynamic response in ultra-high field MRI. Neuroimage 168, 279–295. https://doi.org/10.1016/j.neuroimage.2017.02.063.

Waehnert, M.D., Dinse, J., Weiss, M., Streicher, M.N., Waehnert, P., Geyer, S., Turner, R., Bazin, P.L., 2014. Anatomically motivated modeling of cortical laminae. Neuroimage 93, 210–220. https://doi.org/10.1016/j.neuroimage.2013.03.078.

Waldecker, M., Leckel, M., Rammelsberg, P., Bömicke, W., 2019. Fully digital fabrication of an occlusal device using an intraoral scanner and 3D printing: a dental technique. J. Prosthet. Dent 121, 576–580. https://doi.org/10.1016/j.prosdent.2018.09.021.

Walsh, D.O., Gmitro, aF., Marcellin, M.W., 2000. Adaptive reconstruction of phased array MR imagery. Magn. Reson. Med. 43, 682–690. https://doi.org/10.1002/(SICI)1522-2594(200005)43:5<682::AID-MRM10>3.0.CO;2-G.

Wan, X., Gullberg, G.T., Parker, D.L., Zeng, G.L., 1997. Reduction of geometric and intensity distortions in echo-planar imaging using a multireference scan. Magn. Reson. Med. 37, 932–942. https://doi.org/10.1002/mrm.1910370619.

Weber, B., Keller, A.L., Reichold, J., Logothetis, N.K., 2008. The microvascular system of the striate and extrastriate visual cortex of the macaque. Cerebr. Cortex 18, 2318–2330. https://doi.org/10.1093/cercor/bhm259.

Windischberger, C., Robinson, S., Rauscher, A., Barth, M., Moser, E., 2004. Robust field map generation using a triple-echo acquisition. J. Magn. Reson. Imaging 20, 730–734. https://doi.org/10.1002/jmri.20158.

Yarnykh, V.L., 2007. Actual flip-angle imaging in the pulsed steady state: a method for rapid three-dimensional mapping of the transmitted radiofrequency field. Magn. Reson. Med. 57, 192–200. https://doi.org/10.1002/mrm.21120.

Zaitsev, M., Akin, B., LeVan, P., Knowles, B.R., 2017. Prospective motion correction in functional MRI. Neuroimage 154, 33–42. https://doi.org/10.1016/j.neuroimage.2016.11.014.

Zaitsev, M., Dold, C., Sakas, G., Hennig, J., Speck, O., 2006. Magnetic resonance imaging of freely moving objects: prospective real-time motion correction using an external optical motion tracking system. Neuroimage 31, 1038–1050. https://doi.org/10.1016/j.neuroimage.2006.01.039.

Zaitsev, M., Hennig, J., Speck, O., 2004. Point spread function mapping with parallel imaging techniques and high acceleration factors: fast, robust, and flexible method for echo-planar imaging distortion correction. Magn. Reson. Med. 52, 1156–1166. https://doi.org/10.1002/mrm.20261.

Zeng, H., Constable, R.T., 2002. Image distortion correction in EPI: comparison of field mapping with point spread function mapping. Magn. Reson. Med. 48, 137–146. https://doi.org/10.1002/mrm.10200.